ALMA MATER STUDIORUM
UNIVERSITÀ DI BOLOGNA

ARCHIVIO ISTITUZIONALE
DELLA RICERCA

Alma Mater Studiorum Università di Bologna
Archivio istituzionale della ricerca

Hydrothermal silicification and active extensional faulting: Insights from the Kornos-Aghios Ioannis fault, Lemnos Island, Greece

This is the final peer-reviewed author's accepted manuscript (postprint) of the following publication:

Published Version:
Berio, L.R., Balsamo, F., Lucca, A., Pizzati, M., Storti, F., Aldega, L., et al. (2025). Hydrothermal silicification and active extensional faulting: Insights from the Kornos-Aghios Ioannis fault, Lemnos Island, Greece. GEOLOGICAL SOCIETY OF AMERICA BULLETIN, 137(9-10), 4015-4041 [10.1130/b37810.1].

Availability:
This version is available at: https://hdl.handle.net/11585/1023150 since: 2025-09-13

Published:
DOI: http://doi.org/10.1130/b37810.1

Terms of use:

Some rights reserved. The terms and conditions for the reuse of this version of the manuscript are specified in the publishing policy. For all terms of use and more information see the publisher's website.

This item was downloaded from IRIS Università di Bologna (https://cris.unibo.it/).
When citing, please refer to the published version.

(Article begins on next page)

08 July 2026

Hydrothermal silicification and active extensional faulting: Insights from the Kornos-Aghios Ioannis Fault, Lemnos Island, Greece

L.R. Berio[1*], F. Balsamo[1], A. Lucca[1], M. Pizzati[1], F. Storti[1], L. Aldega[2], A. Cipriani[3,4], L. Dallai[2], F. Lugli[3], L. Mantovani[1], V. Moretto[2], T. Trua[1], S. Zanchetta[5], G. Viola[6]

[1]Università di Parma, Dipartimento di Scienze Chimiche, della Vita e della Sostenibilità Ambientale, NEXT - Natural and Experimental Tectonics Research Group, Parco Area delle Scienze 157/A, 43124, Parma, Italy
[2]Dipartimento di Scienze della Terra, Sapienza Università di Roma, Piazzale Aldo Moro 5, 00185, Roma, Italy
[3]Dipartimento di Scienze Chimiche e Geologiche, Università di Modena e Reggio Emilia, Via Campi 103, 41125, Modena, Italy
[4]Lamont-Doherty Earth Observatory of Columbia University, 61 Route 9W, Palisades, New York 10964, USA
[5]Dipartimento di Scienze dell'Ambiente e della Terra, Università degli Studi di Milano – Bicocca, Piazza della Scienza 4, 20126, Milano, Italy
[6]Università di Bologna, Dipartimento di Scienze Biologiche, Geologiche e Ambientali, Via Zamboni 67, 40126, Bologna, Italy

*Corresponding author: luigiriccardo.berio@unipr.it, +39 3478382188

ABSTRACT

Fault-related diagenesis critically influences the petrophysical and mechanical properties of fault zones, affecting fluid circulation and seismicity in the upper crust. Questions remain about the composition of the mineralizing fluids and the role of fault architecture in controlling the distribution of hydrothermal silicification. This study addresses these questions by establishing the source of hydrothermal fluids and documenting the spatial variability of synkinematic hydrothermal products along the Kornos-Aghios Ioannis Fault (KAIF; Lemnos, Greece). The KAIF is a ~10 km-long extensional fault system that deforms, at shallow depth (<1 km), Eocene-Miocene sandstone turbidites and volcanic rocks. Our multidisciplinary approach, combining structural analysis, petrography, mineralogy, geochemistry, and fluid inclusion microthermometry, revealed that silicification occurred in an epithermal environment assisted by the circulation of acid-sulphate hydrothermal fluids (T≃ 160-170 °C). Mineralizing fluids were predominantly meteoric in origin, with a possible residual magmatic component. The intensity of

silicification decreases with distance from the principal slip surface, forming up to 250 m-thick rock volumes that, locally, outsize the width of the fault damage zone. Along the fault strike, only a ~4 km-long fault segment exhibits silica cementation. This along-strike variability is best explained by the long-term evolution of the fault system. Kilometer scale soft- and hard-linkage patterns combined with second-order geometrical complexities (e.g. breached relay ramps and tips) localized fluid flow and promoted extensive alteration. Our findings have implications upon the understanding of the permeability structure of silica-cemented fault zones, with relevance for the assessment of seismic hazards and exploration of natural resources in siliciclastic rocks.

INTRODUCTION

Fault-related cementation and alteration processes (i.e. porosity reduction/enhancement due to mineral precipitation/dissolution in sedimentary rocks) such as dolomitization, calcite cementation, or silicification have been largely documented in the literature and can significantly modify the petrophysical properties of fault zones (Labaume and Moretti, 2001; Boles et al., 2004; Eichhubl et al., 2009; Sutherland et al., 2012; Laubach et al., 2014; Kristensen et al., 2016; Williams et al., 2017; Menezes et al., 2019; Mozafari et al., 2019; Pizzati et al., 2019; Callahan et al., 2020; Salomon et al., 2020; Palhano et al., 2023). Fault-related cementation has been shown to be complex, depending on several controlling factors such as the mineral composition and petrophysical properties of pristine host rock (Laubach et al., 2014), the occurrence of open vs. closed fluid systems (Kirschner et al., 1999; Travé et al., 2007; Lacroix et al., 2014; Cerchiari et al., 2020), the presence of fluids in thermal equilibrium/disequilibrium with the host rock (Labaume and Moretti, 2001; Boles et al., 2004; Lucca et al., 2018; Smeraglia et al., 2018; Curzi et al., 2024). Moreover, cementation is controlled by the fault architecture (Eichhubl et al., 2009), which, in turn, governs the locus of fluid flow and the continuous vs. episodic fluid regime (e.g., Eichhubl and Boles, 2000; Sibson, 2000; Williams et al., 2017).

In fault zones, rock volumes characterized by the presence of alteration minerals at concentrations higher than background regional levels can be termed “chemical alteration zones” (*sensu* Sutherland et al., 2012; Kristensen et al., 2016). In hydrothermal systems, the development of chemical alteration zones is driven by the circulation of fluids that are appreciably warmer and out of chemical equilibrium with respect to their host rocks. These fluids leach, transport, and subsequently precipitate their mineral load in response to changing chemical and physical

conditions (Machel and Lonnee, 2002; Davies and Smith, 2006; Pirajno, 2009). These hot and less dense fluids may rise up to shallow crustal levels due to buoyancy driven thermal convection which is favored in thick and permeable fault damage zones (e.g., Guillou-Frottier et al., 2024) and in response to topographically driven fluid movements, producing highly anomalous local fluid pressure and temperature gradients (Sutherland et al., 2017).

In hydrothermal environments, silica cements (e.g., amorphous silica, chalcedony, microcrystalline quartz, and quartz) commonly precipitate in structurally-controlled domains from supersaturated silica-bearing fluids derived from igneous intrusion, deep convection of meteoric fluids, or metamorphic devolatilization (Essarraj et al., 2001; Pirajno, 2009; Bonnemains et al., 2017; Verlaguet et al., 2021), with silica precipitation driven by rapid cooling and/or lowering pH (Fournier, 1985). In magmatic-hydrothermal systems, such as porphyry and epithermal systems, fluid composition can be variable because early magmatic-hydrothermal fluids, typically highly saline to hypersaline, are generally succeeded by convective meteoric-derived hydrothermal fluids, with which they mix until the magmatic component completely disappears (Pirajno, 2009). Interactions between hot and highly reactive hydrothermal fluids and host rocks may potentially produce different types of hydrothermal alterations by mineral dissolution and precipitation along structural elements and within pores (Papoulis and Tsolis-Katagas, 2008; Ece et al., 2013; Börner et al., 2022; Hedenquist and Arribas, 2022; Marchesini et al., 2024). Furthermore, in low-porosity silicified rocks, transient fluid pressure variations along specific fault patches and segments may generate volumes of hydraulic breccias of potential economic interest for mineral exploration (Jébrak, 1997; Voudouris and Alfieris, 2005; Caine et al., 2010; Grare et al., 2018; Mazzarini et al., 2019; Bezerra et al., 2021; Cazarin et al., 2021; Gülyüz et al., 2023). These processes of hydrothermal silicification, alteration and brecciation are known to occur cyclically during fault growth history (e.g., Sibson, 1981; Caine et al., 2010) and, as such, play a key role in controlling the evolution of petrophysical and mechanical properties of fault rocks with implications for fault strength and fluid circulation in fault damage zones (Caine et al., 2010; Callahan et al., 2019, 2020; Menezes et al., 2019; Fernandez-Ibanez et al., 2022; de Jesus et al., 2023; Palhano et al., 2023) and for seismicity in the upper crust (Caine et al., 2010; Sutherland et al., 2012; Bezerra et al., 2021).

Understanding the along- and across-fault strike variability of the hydrothermal products and its impact on primary and fracture porosity has implications on many industrial applications,

such as subsurface fluid storage, geothermal production and the exploitation of hydrothermal mineral deposits (Faulkner et al., 2010; You et al., 2018; Lima et al., 2020; Liotta et al., 2021, 2023; Fernandez-Ibanez et al., 2022). Consequently, the space-time evolution of hydrothermal processes and the geometric variability of alteration products are of great importance for two major reasons: (1) hydrothermally altered and silicified zones can be significantly heterogeneous at the reservoir scale (e.g., You et al., 2018; Lima et al., 2020), (2) hydrothermally altered and silicified zones can have contrasting effects on the petrophysical and mechanical properties of fault rocks (You et al., 2018; Callahan et al., 2019, 2020; Menezes et al., 2019; Palhano et al., 2023), with implications for the accumulation and spatial distribution of damage (e.g., Berio et al., 2023). Despite the availability of several case studies, how fault-related hydrothermal alteration and silicification may vary over distances between tens to thousands of meters is difficult to accurately constrain because of poorly resolved subsurface datasets or limited exposures of field outcrop analogues.

The study of the structurally segmented and hydrothermally altered and silicified Kornos-Aghios Ioannis Fault (KAIF) (**Fig. 1A**), which deformed siliciclastic turbidites and volcanic rocks by accommodating hundreds of meters of extensional displacement at shallow burial depth (< 1 km; Berio et al., 2023) in a porphyry-epithermal system (Voudouris and Alfieris, 2005; Papoulis and Tsolis-Katagas, 2008; Börner et al., 2022), was designed to address the following questions: (1) Are hydrothermal alteration products evenly distributed along a segmented fault system? What are the structural and stratigraphic factors that may control, at different dimensional scales, their along- and across-strike distribution? (2) Inside the hydrothermally altered and silicified fault zone, are the mineralogy and textures homogeneous or heterogeneous? Is there any trend in mineral composition moving from the principal slip surface to the host rock? (3) Is the thickness of hydrothermal silicification and alteration smaller or greater than that of fault damage zone? Is the boundary between silicified and host rocks abrupt or gradual? (4) Do hydrothermal fluids responsible for silicification and alteration have a dominant magmatic or meteoric origin? And what is the source of silica in large-scale silicified faults?

To address these questions, we integrated detailed field mapping of the hydrothermally altered and silicified rocks along the well-exposed ~10 km-long extensional fault system with petrography, microstructural analysis, X-ray diffraction mineralogy, stable isotope geochemistry, and fluid inclusion microthermometry of diagenetic products.

GEOLOGICAL SETTING

Regional Stratigraphic-Tectonic Framework

The Aegean region in the Eastern Mediterranean Sea evolved as part of a convergent plate margin above the north-dipping Hellenic subduction zone, which produced an orogenic system characterized by the stacking of large tectonic nappes (e.g., Taymaz et al., 2007; Jolivet et al., 2013). Thickened lithospheric domains were later affected by syn- to post-orogenic extension (Jolivet et al., 1994, 2018) driven by the gravitational instability of the Hellenic orogenic wedge and by the southward migration of the subduction system (Bonev and Beccaletto, 2007; Jolivet and Brun, 2010; Jolivet et al., 2013). In the North Aegean region, Late Cenozoic extension and exhumation were accompanied by a widespread Miocene post-subduction magmatism resulting in calc-alkaline and shoshonitic plutonic and volcanic rocks (Pe-Piper et al., 2009) and by Eocene-Miocene sedimentation in several subsiding depocenters (Siyako and Huvaz, 2007; Innocenti et al., 2009; Caracciolo et al., 2011).

A clastic sedimentary sequence deposited in the western Thrace Basin is well exposed on Lemnos Island (Innocenti et al., 1994, 2009; Caracciolo et al., 2011; Maravelis et al., 2015). The sequence includes Middle-Upper Eocene to Lower Miocene deep marine turbidite deposits (Fissini-Sardes and Ifestia Units) unconformably overlain by shallow marine to continental deposits (Therma Unit) (**Fig. 1A, B**). This sedimentary sequence has a maximum thickness of ca. 500 m and experienced shallow burial (T max < 70 °C)(Caracciolo et al., 2011; Perri et al., 2016). It is intruded and partly covered by the Early Miocene calc-alkaline to shoshonitic effusive and hypabyssal magmatic rocks of the Romanou, Katalakkon and Myrina Units (Innocenti et al., 2009; Pe-Piper et al., 2009; **Fig. 1A, B**). Pliocene-Quaternary continental deposits locally cover the area (Innocenti et al., 1994, 2009)

Lemnos Island is located within a seismically active region (e.g., Pavlides et al., 1990, 2009), ~ 25 km to the south of the North Aegean Trough, a narrow and highly subsiding ENE-WSW transtensional domain that represents the westward extension of the North Anatolian Fault (NAF; Pavlides et al., 1990; Taymaz et al., 1991; Armijo et al., 1999; Koukouvelas and Aydin, 2002). ENE-WSW to NE-SW branches of the NAF also characterize the East Aegean Sea 30-40 km to

158 the south of Lemnos as attested to by recent seismicity and strike-slip focal mechanism solutions
159 (Pavlides and Tranos, 1991; Caputo et al., 2012; Kiratzi and Svigkas, 2013; inset in **Fig. 1A**).
160
161 **The Kornos-Aghios Ioannis Fault (KAIF): Architecture in Map View**
162
163 On Lemnos Island, the KAIF is the best developed fault system and has a ~NW-SE mean
164 azimuthal trend, whereas the majority of fault zones strike E-W and ENE-WSW (Tranos, 2009;
165 Berio et al., 2023; **Fig. 1A, C**). The KAIF is a SW-dipping, segmented extensional fault system
166 with an onshore total length of ~10 km and an unknown throw (Innocenti et al., 2009; Berio et al.,
167 2023). A rough estimation of throw using displacement-length and displacement-damage zone
168 width scaling relationships for siliciclastic rocks (Torabi and Berg, 2011; Berio et al., 2023) yields
169 values in the order of hundreds of meters. Deformed rock volumes are locally affected by intense
170 hydrothermal alteration and silicification (Papoulis and Tsolis-Katagas, 2008; Fornadel et al.,
171 2012; Anifadi et al., 2017; Berio et al., 2023).
172 In map view, the KAIF consists of two major NW-SE-trending overlapping fault segments
173 connected by an E-W breaching fault (Berio et al., 2023; **Fig. 1C**). The hanging wall of the KAIF
174 consists of the turbidites of the Ifestia Unit intruded by the hypabyssal rocks of the Myrina Unit.
175 In the footwall, turbidites of the Fissini-Sardes Unit and the dacite intrusions of the northern
176 Katalakkon Unit are exposed.
177 The northern NW-SE fault segment (sectors A, B) extends for ~4 km and has tip regions
178 characterized by several splays (**Fig. 1C**). In the northwestern portion of sector A, the tip region is
179 characterized by curved fault splays forming a horse tail geometry. The E-W breaching fault
180 segment (sector C) extends for ~1.5 km and connects the two main NW-SE fault segments. The
181 southern NW-SE-trending fault segment (Sector D) is ~3 km long. The principal slip surface in
182 the latter sector is poorly exposed as it is generally covered by vegetation.
183 Principal slip surfaces have striae and grooves indicating dip-slip movements (Berio et al.,
184 2023). The mean attitude of principal slip surfaces in sectors A, B and C is 116/67 (n=163), 116/63
185 (n=277) and 87/71 (n=67), respectively (structural data reported as strike-dip angle, following the
186 right-hand rule). Slickenlines indicate predominant dip-slip motions in all the segments, with mean
187 pitch values of 85° ± 19° (n=94), 92° ± 14° (n=207) and 93° ± 17° (n=43), respectively (stereonets
188 in **Fig. 1C**).

METHODS

Structural Mapping and Sampling Strategy

Our detailed 1:500 scale structural mapping covered the central and western portion of the KAIF, where the structure and hydrothermal alteration are best exposed. Structural analysis and mapping allowed us to (i) reconstruct the overall structural architecture of the KAIF, (ii) propose a classification of the hydrothermally altered fault-related rocks, and (iii) select suitable samples for microstructural, geochemical and mineralogical investigations. At the outcrop scale, different types of hydrothermally altered fault-related rocks were identified, based on the deformational characteristics and the cement types. Such classification was further confirmed by optical petrography and X-ray diffraction.

A total of 102 samples were collected from different sites along the KAIF. The geographical coordinates and the location of the sampling sites are reported in the Supplemental Material[1] (**Table S1**) and in **Fig. 1C**, respectively. The samples are representative of a variety of host rocks and hydrothermally altered fault-related rocks (mostly damage zone veins and fault core ultracataclasite, cataclasite and breccia with different degree of alteration and cementation) and were collected for petrography, microstructural analysis, geochemistry, X-ray diffraction mineralogy, and fluid inclusion microthermometry (see sampling sites in **Fig. 1A, C**). Two samples of unaltered host rock were collected far away from the study area, to compare and contrast their whole-rock composition with that of the silicified rocks, as to exclude any possible effect of thermal anomalies caused by fluid circulation along the fault zones and/or by volcanic activity (red star in **Fig. 1A**).

Detailed analytical procedures for optical microscopy and cathodoluminescence analysis, SEM, X-ray diffraction, laser ablation inductively coupled mass spectrometry (LA-ICP-MS), stable isotope analysis and fluid inclusion microthermometry are reported in the **APPENDIX**.

RESULTS

Overview of the Hydrothermally Altered KAIF

In cross section, the studied fault zone structure consists of a meter-thick fault core surrounded by fractured damage zones developed both in the hanging wall and footwall blocks

(**Fig. 2**). The fault core is bounded on one side by a remarkably continuous, polished principal slip surface (**Fig. 2A**). Damage zones contain synthetic and antithetic extensional faults, joints and rare veins that invariably cut across the hydrothermally altered and silicified fault-related rocks. The overall fault zone thickness varies along fault strike between ~80 and ~120 m in the tip region of sector A, where it attains its maximum width (Berio et al., 2023). Outside of fault damage zones, turbidite sandstones gently dip (10-30°) towards N-NW both in the hanging wall and in the footwall (**Fig. 1C**). Approaching the principal slip surface, turbidite beds in the footwall are characterized by progressively steeper attitudes and, at 2-3 m from the principal slip surface, they are sub-parallel to it (**Fig. 2A, B**).

Hydrothermally altered and silicified fault-related rocks occur only in sectors A and B, over a distance of at least 3-4 km along the fault strike (**Fig. 1C**). In the hydrothermally altered sectors, hydrothermal fluids permeated only siliciclastic units both in the hanging wall and in the footwall (**Fig. 2A-B**). Sectors C and D are not affected by hydrothermal alteration and silicification (**Fig. 1C**).

At the outcrop scale, fault-related hydrothermal alteration and silicification are marked by a pronounced positive relief due to the erosional contrast with respect to the country rocks (**Fig. 2A-B**). In cross section, typically fault zones in sandstones are completely hydrothermally altered and silicified (**Fig. 2A**), although, in some cases, the hydrothermally altered bodies are irregular and exhibit a patchy distribution (**Fig. 2B**). The thickness of the across-fault hydrothermal alteration and silicification ranges broadly between ~50 and ~280 m (i.e. the hydrothermally altered and silicified zone is locally much greater than the damage zone width).

Classification of Hydrothermally Altered Fault-Related Rocks

Turbidite host rocks outside fault zones consist of light brown to orange coarse-to medium-grained sandstones and interbedded laminated grey colored mudstones (**Fig. 3A**). Host rock sandstones are composed of lithic fragments (metamorphic, igneous and sedimentary), feldspar and quartz grains. The host volcanic rocks are porphyritic, with phenocrysts of plagioclase, K-feldspar, biotite, and amphibole resembling the dacites of the Aghios Ioannis subunit and the Katalakkon unit (Pe-Piper et al., 2009). Hydrothermally altered fault-related rocks consist of: (i) massively silicified sandstones (**Fig. 3B**); (ii) massively silicified fault core rocks (**Fig. 3C**), i.e. mostly cataclasites and ultracataclasites and subordinate breccias; (iii) argillitic-altered sandstones

(**Fig. 3D**); (iv) quartz-cemented crackle breccias (**Fig. 3E**); (v) partially-silicified to non-silicified fault core rocks (**Figs. 3F, 4A**), i.e. poorly cohesive cataclasites and gouges; and (vi) vein stockworks (**Fig. 4B, C**). Main features of these fault-related rock types are described below:

i. Massively silicified sandstones

Massively silicified turbidite sandstones are the volumetrically most significant alteration product. They consist of silicified sandstone strata and mudstone interlayers in fault damage zones (**Fig. 3B**) and, locally, also outside the damage zone (i.e., moving away from the damage zone boundary towards the host rock).

ii. Massively silicified fault core rocks

This category of fault rocks is represented by fully silicified ultracataclasites and cataclasites, and locally by silicified fault breccias (**Fig. 3C**). Massively silicified cataclasites and ultracataclasites preserve an increasing comminution gradient approaching the principal slip surface and contain a well-developed foliation sub-parallel to the principal slip surface (**Fig. 3C**). They are characterized by very low porosity and commonly contain clasts of silica that are embedded in a silicified cataclastic matrix (**Fig. 3C**).

iii. Argillic-altered turbidite sandstones

Argillic-altered turbidites (fine- to medium-grained sandstone beds) are made of sandstone strata and mudstone interlayers affected by advanced argillic alteration (**Fig. 3D**), mostly preserved within fault zones as 1-10 m-thick, whitish irregular pods that are generally surrounded by massively silicified sandstone with scalloped boundaries. Argillic-altered turbidite strata are extensively micro-fractured, locally forming centimeter-scale micro-breccia pockets cemented by silica and iron oxides (**Fig. 3D**). Clasts in the micro-breccias are mm in size and very angular (**Fig. 3D**).

iv. Quartz-cemented crackle breccias

Quartz-cemented crackle breccias form mostly in fault damage zones at the expense of the massively silicified sandstones (**Fig. 3E**). Subordinately, they also overprint the argillic-altered sandstones (**Fig. 3D**) and the silicified fault core rocks, at the contact with principal

slip surfaces. Fracture meshes of crackle breccias are cemented by a combination of silica and quartz and are frequently characterized by mm- to cm-sized vuggy porosity in geodes/druses, partially filled by iron oxides/hydroxides (**Fig. 3E)**. Vuggy porosity and sandstone clasts are rimmed by red haloes of iron oxides (**Fig. 3E**). Clasts are cm to dm in size, with low sphericity and high aspect ratios (**Fig. 3E**).

v. Partially silicified to non-silicified fault core rocks

Partially silicified to non-silicified fault core rocks consist of poorly cohesive fault breccias, cataclasites, and gouges (**Figs. 3F, 4A**). These fault rocks vary in color from white to red and form bands up to 1.5 m in thickness (**Fig. 4A**), which are foliated and generally characterized by an immature cataclastic texture (**Figs. 3F, 4A**). Where the fault zone is silicified, they are invariably bounded on one side by striated silicified fault rocks or sandwiched between them (**Fig. 4A**). Partially silicified to non-silicified fault core rocks clearly post-date the massive silicification since they contain clasts of massively silicified sandstones and fault core rocks (**Fig. 3F**). For instance, partially silicified fault breccias commonly contain cm-sized clasts of previously silicified cataclasite that are dispersed within a partially silicified cataclastic matrix (**Fig. 3F**).

vi. Vein stockworks (VS)

In hanging wall and footwall damage zones, volcanic and siliciclastic rocks are locally affected by randomly oriented fractures, cemented by quartz, micro-crystalline quartz, calcite, barite, dolomite and iron oxides (**Fig. 4B, C**). Vein apertures vary between 0.5 mm to 7 cm (**Figs. 4B, C**). Such vein stockworks affect both host rocks and previously silicified fault-related rocks. In the veins, minor occurrences of barite are typically associated with abundant calcite, whereas dolomite is associated with quartz (**Fig. 4C**).

Along-Fault Distribution and Thickness of Hydrothermally Altered Fault-Related Rocks

Massively silicified turbidite sandstones extend horizontally from the principal slip surface up to 250 m in the footwall and, only locally, up to 25-30 m in the hanging wall even if the latter measurement may be an underestimation because of the limited exposure of the hanging wall block

(**Figs. 5A, 6**). These silicified domains are locally thicker than the fault damage zones (cfr. Berio et al., 2023; **Fig. 6A**). In the turbidite, massive silicification preferentially affects the medium-grained sandstone compared to mudstone layers. Massively silicified fault core rocks extend up to 3 m from the principal slip surface and form tabular to elongated irregular bodies strongly resistant to erosion (**Fig. 5B**).

Argillic-altered sandstones characterize the northern tip-region of the KAIF (**Fig. 6A**). More specifically, argillic-altered sandstones are sandwiched between two major fault strands forming the extensional horsetail of sector A and they are in tectonic contact with the the Katalakkon unit towards NNE and with the Myrina Unit towards SSW (**Figs. 5B, 6A**). In the 50 m-wide fault-bounded slice of argillic-altered sandstones, bedding is still visible and dips towards SSE, while progressively increasing the dip angle approaching the southern fault strand, where the argillic-altered sandstones are subordinate to massively silicified sandstones and quartz-cemented crackle breccias (**Figs. 5B, 6A**).

Quartz-cemented crackle breccias typically occur in domains that extend up to 70-80 m in the footwall block (**Figs. 5A, 6**). Brecciated domains always develop on previously silicified sandstones and, typically, are a few meters thinner than the latter (**Fig. 6B**).

Petrography and Microstructures of Hydrothermally Altered Fault-Related Rocks

In massively silicified sandstones, the primary porosity is occluded to various degrees by silica cements compared to non-silicified ones, where primary porosity is partially preserved (**Fig. 7A-B**). Silica cements in silicified sandstones occur as microcrystalline quartz or as large crystals with euhedral habit (**Fig. 7C-D**). Pyrite in euhedral prismatic crystals occurs with microcrystalline quartz (**Fig. 7C**). Clay minerals along the detrital grain margins form coatings that always pre-date quartz cementation (**Fig. 7 C-D**). Quartz overgrowths in optical continuity with the detrital cores are locally observed, but their development is frequently prevented by clay mineral coatings.

Massively silicified fault core rocks are predominantly made up of microcrystalline quartz + quartz + pyrite + relict feldspar (**Fig. 8A-B**). Microcrystalline quartz + quartz is the most widespread association of silica cements in the silicified fault core rocks both in clasts and in matrix (**Fig. 8A-B**). Silica phases, such as amorphous silica (opal-A), opal-CT and chalcedony, are rarely observed since they are converted to microcrystalline quartz and quartz. Silica cements are systematically cross-cut by micro veins filled by iron oxides – hydroxides (**Fig. 8C**).

As already evident at the mesoscale (**Fig. 3C-D**), silicified fault core rocks contain clasts of silicified sandstones embedded within a silicified cataclastic matrix (**Fig. 8D-E**). Moreover, silicified fault core rocks are in turn reworked by later silicified cataclasites attesting to multiple silicification phases alternating with brecciation and cataclasis (**Fig. 8E**). At the microscale, clasts of silicified sandstones and cataclasites appear as having been silicified before renewed episodes of cataclasis. This is for the following reasons: (i) their boundaries are still visible, (ii) there is no mineral continuity between clasts and matrix, (iii) not all the clasts are silicified (**Fig. 8D**). The outer margins of clasts of silicified sandstones and cataclasites are commonly irregular and exhibit smooth embayments caused by corrosion and dissolution during the later silicification phase (**Fig. 8E**). On principal slip surfaces, truncated sandstone clasts on sharp slip surfaces in massively silicified fault core rocks were observed (**Fig. 8F**). Principal slip surfaces are typically coated by microcrystalline silica between 100 μm to 1 mm in thickness (**Fig. 8F**).

Massively silicified turbidite sandstones in the damage zones are brecciated and cemented by quartz in euhedral crystals mm to cm in size with feathery textures and microcrystalline quartz (**Fig. 9A, B**). Massively silicified cataclasites and ultracataclasites are brecciated and cemented by quartz in euhedral crystals mm to cm in size and microcrystalline quartz (**Fig. 9C**). These breccias on principal slip surfaces contain fragments of silicified fault rocks that are mm to cm in size and are characterized by low sphericity and high aspect ratios, and exhibit high cement/fragment ratios (**Fig. 9C**). They do not exhibit evidence for cataclastic flow such as clast rounding and comminution. Vuggy porosity in quartz-cemented crackle breccias is partially filled by iron oxides/hydroxides (**Fig. 9A, C**). The massively silicified cataclasites and ultracataclasites are cross-cut by veins and microveins filled by microcrystalline silica and quartz and by younger veins cemented by iron oxides/hydroxides (**Fig. 9C, D**). In the veins, mineral phases precipitated following the sequence microcrystalline silica - quartz (**Fig. 9D**).

While the massively silicified fault core rocks are reworked by multiple faulting episodes, younger fault cores are unaffected or only partially affected by silicification (**Fig. 10A**). These fault cores are commonly mineralized by iron oxides/hydroxides (lepidocrocite/goethite) and K-bearing micas (**Fig. 10B**). K-bearing micas occur as flaky millimetric crystals that in plane polarized light appear concentrically zoned around vuggy porosity with colors between orange and brown (**Fig. 10C**). They grew synchronously with quartz (**Fig. 10C**). Fault core sectors mineralized

by iron oxides and hydroxides and cogenetic quartz are highly porous and have gradual contacts with sectors mineralized by K-bearing mica + quartz (**Fig. 10D**).

Stockwork veins in fault damage zones are commonly cemented by quartz, calcite + barite and quartz + dolomite (**Fig. 11**). Quartz is characterized by elongated crystals that range in size from 100 to 5000 μm and grew perpendicularly to the vein walls. Frequently, syntaxial veins are not completely sealed by quartz cement and the remaining porosity is partially filled by iron-oxides. Several micro-veins (100 μm to 500 μm wide) cemented by iron-oxides cross-cut quartz-filled veins (**Fig. 11A**).

Calcite typically occurs in twinned blocky crystals (500 to 4000 μm in size) and is intimately intergrown with bladed crystals with very high length-width ratios (up to 80). Barite crystals ranging in size from 500 to 3000 μm grew together with calcite ones (**Fig. 11B**). CL imaging indicates that bladed crystals are more luminescent than the blocky ones, with bright yellow colors. Blocky crystals between the bladed ones exhibit a zoned luminescence pattern, with alternating bright yellow and pale orange colors (**Fig. 11C**). In some veins, calcite crystals are fibrous and exhibit crack-seal microstructures, highlighted by host-rock inclusion trails. Dolomite occurs mostly as rhombohedral crystals characterized by a dull red luminescence and up to 500 μm in size intergrown with microcrystalline quartz and calcite (**Fig. 11D**). Rhombohedral dolomite crystals can be dispersed in a siliceous matrix made of microcrystalline silica.

X-ray Diffraction of Hydrothermally Altered Fault-Related Rocks and Host Rocks

Mineralogical data from whole-rock and from the <2 μm grain-size fraction are summarized in **Table 1 and Table 2**, respectively. Mudstone layers from the host rock (samples S18, S128) are mostly composed of phyllosilicates, calcite, and quartz, with subordinate amounts of dolomite, goethite, albite, and K-feldspar traces (**Table 1**). In the <2 μm grain size fraction, illite is the prevailing clay mineral, followed by chlorite, mixed I-S layers, and kaolinite. Mixed I-S layers correspond to randomly ordered structures (R0) with an illite content of 30 wt. %. Whole-rock data of sandstone layers from the host rock (samples OK7, PK11), when compared to mudstone layers, show lower contents of phyllosilicates and higher contents of quartz and feldspars (**Table 1**).

Whole-rock data of partially silicified to non-silicified fault core rocks (samples SG33, SG34, KORK5, KORK6, and KORK7) show phyllosilicate contents similar to those obtained from

404 undeformed mudstone layers with higher quartz contents, followed by K-feldspar, goethite, and
405 anatase (**Table 1**). Traces of dolomite, halite, and apatite, occur sporadically. In the <2 μm grain
406 size fraction, clay mineral assemblages are dominated by illite and mixed I-S layers (**Table 2**).
407 Mixed I-S layers correspond to long-range ordered structures (R3) with illite contents varying
408 between 85 and 90 wt. % (**Table 2**).
409 Whole-rock data of massively silicified fault core rocks (samples OK1 and PK1) display
410 quartz and k-feldspar with low contents of phyllosilicates and albite (**Table 1**). Quartz-cemented
411 crackle breccias (sample OK4) are predominantly composed of quartz, with albite, K-feldspar and
412 phyllosilicates (**Table 1**). Argillic altered turbidite sandstones (sample PA3A) are composed of
413 quartz and phyllosilicates (**Table 1**).
414 Massively silicified sandstones are characterized by a strong compositional variability in
415 the footwall, which relies on the distance from the principal slip surface (**Fig. 12; Table 1**). The
416 mineralogical variability of the silicified sandstones has been investigated in two across fault
417 transects located in different positions along-strike (**Fig. 1C**). The transect in sector B shows that
418 the quartz content steadily remains above 80 wt. % up to a distance of ca. 40 m from the principal
419 slip surface and then progressively decreases. Moving away from the principal slip surface along
420 the same transect, the K-feldspar content does not significantly vary, phyllosilicates slightly
421 increase, and plagioclase inversely follows the quartz trend (**Fig. 12A**). The transect in sector A
422 shows less regular mineralogical trends. Quartz content irregularly varies between 47 and 88 wt.
423 % irrespectively of the distance from the fault principal slip surface, but from a distance of ca. 60
424 m it does not decrease below 64 wt. % (**Fig. 12B**). K-feldspar and plagioclase inversely follow the
425 quartz trend, whereas muscovite positively follows it (**Fig. 12B**).
426
427 **Fluid Inclusion Microthermometry of Calcite and Silica Cements**
428 Fluid inclusion analysis was performed on calcite- (**Figs. 4B-C, 11B-C**) and quartz-filled
429 veins (**Fig. 11A**), and on quartz-cemented crackle breccias (**Figs. 3D-E, 9A-C**). Both in calcite
430 and quartz crystals, only primary inclusions were selected for microthermometry. In calcite,
431 primary fluid inclusions are preferentially found in domains parallel to crystal boundaries, in which
432 fluid inclusion density is higher (**Fig. 13A**). In such cases, inclusions have their long axes
433 preferentially oriented parallel to growth zones (**Fig. 13A-B**). In quartz, selected primary
434 inclusions are preferentially concentrated in crystal cores surrounded by clearer rims. Primary fluid

inclusions vary in size between 4 to 20 μm and their shape ranges from irregular to equant. In calcite crystals, inclusions have preferentially rectangular to prismatic shapes and negative crystal morphologies have been observed (**Fig. 13B**). In quartz crystals, fluid inclusion shapes range from subrounded to rectangular. Fluid inclusions are two-phase liquid-vapor inclusions, with liquid to vapor ratios varying between 5 and 20% (**Fig. 13B**). Isolated inclusions were disregarded and only fluid inclusion assemblages (FIAs) with consistent liquid-to-vapor proportions were selected for microthermometry (**Fig. 13B**) (Goldstein and Reynolds, 1994). In five selected samples (**Fig. 1C** for sample location), a total of 109 inclusions were measured, distributed in 21 selected FIAs (**Fig. 13C-D**). Fluid inclusions hosted in calcite crystals show a mean homogenization temperature of 166 ± 17 °C (**Fig. 13C, Table 3**). Fluid inclusions hosted in quartz crystals provided a mean homogenization temperature of 170 ± 16 °C (**Fig. 13C, Table 3**). During freezing runs, bubbles gradually became smaller and were deformed by the growth of ice crystals. In quartz and calcite, a complete freezing of the inclusions was detected by a sudden bubble movement (jerk) at a mean temperature of -41 °C. In many cases in samples KOR2.2D, KOR2.4D and SG25A, two jerks of the bubble have been observed during cooling: the first one may be caused by the formation of solid gas-hydrates (clathrates) and the second one by the complete freezing of the inclusion (Goldstein and Reynolds, 1994). The presence of small amounts of unobservable clathrates is further confirmed by the Tm_{cla} above 0 °C measured in some fluid inclusions both in quartz and calcite. In fact, Tm_{cla} in calcite and quartz ranges between -1.5 and +15.9 with a mean value of 0.7 °C (**Fig. 13D, Table 3**). Tm_{ice} from inclusions free of clathrates (samples SG3 and SG15) ranges between -1.5 and -0.2 with a mean value of -0.7 which corresponds to a mean salinity of 1.23 eq. wt% NaCl (Bodnar, 1993).

Isotopic Data

$\delta^{18}O$ and $\delta^{13}C$ of Calcite and Silica Cements

Carbon and oxygen stable isotope data are reported in **Figure 15** and summarized in **Table 4.** The $\delta^{18}O$ values of vein filling calcite cements from the vein stockworks (VS) have a mean value of -20.2 ‰ V-PDB (**Fig. 14A, Table 4**). Noteworthy is that the $\delta^{13}C$ values of the same calcite cements have a mean value of -3.0 ‰ V-PDB (**Fig. 14A, Table 4**). The $\delta^{13}C$ (‰ V-PDB) values from calcite cements are always negative with only an outlier (**Fig. 14A**). Oxygen stable

isotope data from silica cements (quartz and micro-quartz) sampled in different hydrothermally altered fault-related rocks have a mean value of 8.9 ‰ SMOW (**Fig. 14B, Table 4**). Euhedral quartz cements have $\delta^{18}O$ values in the range from 7.0 ‰ to 7.8 ‰ SMOW, which is slightly lower than the $\delta^{18}O$ range of microcrystalline quartz (from 8.6 ‰ to 12.4 ‰ SMOW). Assuming equilibrium precipitation and using mean fluid temperatures from fluid inclusion microthermometry, the $\delta^{18}O$ values of the parental fluid was calculated for calcite and silica cements, using the equations of O'Neil et al. (1969) and Clayton et al. (1972), respectively. The results are reported in **figure 14C-D** and summarized in **Table 4.** The $\delta^{18}O$ of the fluid calculated from calcite cements has a mean value of -1.5 ‰ SMOW (**Fig. 14C, Table 4**). The $\delta^{18}O$ of the fluid calculated from silica cements has a mean value of -4.9 ‰ SMOW (**Fig. 14D, Table 4**).

δD of Partially Silicified to Non-Silicified Fault Core Rocks and Host Rocks

The δD of partially silicified to non-silicified fault core rocks and host rocks are reported in **Table 5**. The host rocks have a mean δD value of -86.5‰ SMOW from which the value for the fluid has been calculated (mean value -81.15 ‰ SMOW). The corresponding <2 μm grain size fractions have mean δD values of -71.1% SMOW with a calculated δD for the fluid of -64‰ SMOW. Partially silicified to non-silicified fault core rocks have δD values lower than the host rocks with a mean value of -103.82 ‰ SMOW from which the value for the fluid has been calculated (mean value -99.1 ‰ SMOW). Their <2 μm grain size fraction has a mean δD value of -80.12 ‰ SMOW at which corresponds a value for the fluid of -75 ‰ SMOW.

Elemental and REE Composition of Vein Calcite Cements

The Mg, Mn, Fe and Sr concentrations of vein filling calcite cements sampled in the hanging wall damage zone vein stockworks (VS) are reported in **Figure 15A**. Calcite cements are characterized by Mg contents between 345 and 8,113 μg/g, Mn contents between 313 and 8,384 μg/g, Fe contents between 302 and 2,152 μg/g and Sr contents between 1,164 and 11,213 μg/g (**Fig. 15A**).

Vein filling calcite and dolomite cements contain ΣREE ranging from 7 to 459 μg/g. When normalized to chondrite (McDonough and Sun, 1995), the REE profiles of the calcite cements can be divided in two groups. For one group the REE are characterized by steeply inclined patterns

from La to Sm, marked positive Eu anomalies and more or less pronounced humps from Gd to Lu (**Fig. 15B**). The second group is characterized by convex-upward patterns lacking positive Eu anomalies (**Fig. 15C**). The calcites of the first group are all blocky crystals, while the second group is associated with acicular crystals (**Figs. 11C, 15B-C**). Three different chondrite-normalized REE patterns can be recognized for dolomite cements: i) LREE enriched and HREE depleted patterns, but less steep than blocky calcite, with positive Eu anomaly, ii) highly LREE enriched patterns with no Eu anomaly, iii) convex-upward patterns lacking positive Eu anomalies, similar to those of acicular calcite (**Fig. 15C**). The chondrite-normalized patterns of the volcanic rocks of the Myrina and Aghios Ioannis Unit (data from Pe-Piper et al., 2009) are enriched in LREE with respect to HREE and fall within the field of variability of the vein filling calcite and dolomite cements (**Fig. 15D**).

DISCUSSION

Hydrothermal Alteration and Silicification along the KAIF

Fluid Temperature and Composition

Temperature-dependent clay minerals of host rock collected far from the KAIF, other fault zones and volcanic bodies (**Fig. 1A**), indicate that the turbidite mudstone layers exposed in Lemnos Island (Fissini-Sardes and Ifestia Units) experienced maximum burial < 1 km (30 % I in I-S mixed layers; **Table 2**). These data are consistent with published vitrinite reflectance values (R0 0.41 %) from the same formation, which approximately correspond to paleo-temperatures of ca 70 °C (Perri et al., 2016). Unfortunately, the poorly constrained local stratigraphic framework did not allow to estimate the exact stratigraphic distance of the investigated mudstone layers from host rock with respect to the stratigraphic interval involved in deformation along the KAIF. However, it is worth noting that the overall thickness of the turbidite sequence exposed in Lemnos is < 500 m (Maravelis et al., 2015, 2016), implying that burial temperatures of these two sites can not differ more than 10-30 °C depending on the adopted paleo-geothermal gradient (Kolawole and Evenick, 2023).

In sedimentary basins, it remains a matter of debate how to define a fluid as hydrothermal (Lima et al., 2020 and references therein). A possible solution is to base the definition on host rock and fluid paleo-temperature (e.g., Machel and Lonnee, 2002; Davies and Smith, 2006), considering

526 as hydrothermal a fluid that is 5-10 °C warmer than the host rock where it circulates (Machel and
527 Lonnee, 2002). In our case, homogenization temperatures obtained from primary fluid inclusions
528 in carbonate and silica cements suggest minimum fluid temperatures of 166 ± 17 and 170 ± 16 °C,
529 respectively, which are ~ 100 °C higher than those expected for a fluid in thermal equilibrium at
530 maximum burial depth (maximum burial temperature ca 70 °C). The temperature range based on
531 fluid inclusion microthermometry is further confirmed by long-range ordered I-S layers observed
532 in fault cores through which hydrothermal fluid circulated, which supports fluid paleo-
533 temperatures > 160 °C (90% I in I-S mixed layers; **Table 2**). These paleo-temperature values fall
534 in the range of those estimated for hydrothermal fluids circulating within fault zones and fractures
535 in Lemnos Island (100-270 °C) based on mineral assemblages in hydrothermal alteration zones
536 (Papoulis and Tsolis-Katagas, 2008).
537 Fault-related hydrothermal cementation along the KAIF occurred in a porphyry-epithermal
538 system (Voudouris and Alfieris, 2005; Papoulis and Tsolis-Katagas, 2008; Börner et al., 2022), as
539 also constrained by diagnostic mineral textures (**Fig. 11C**), the presence of typically hydrothermal
540 minerals such as pyrite, anatase, and barite (**Figs. 8A, 11B; Table 1, 2**), and by the geochemistry
541 of the calcite cements (**Fig. 15**). Bladed calcite crystal morphologies eventually replaced by silica
542 are indeed indicative of precipitation in epithermal systems (Dong et al., 1995; Jones and Renaut,
543 1998; Pirajno, 2009; Grare et al., 2018; Callahan et al., 2019) (**Fig. 11B-C**). This calcite crystal
544 morphology may be related to rapid CO_2 degassing and to precipitation from a boiling fluid (Jones
545 and Renaut, 1998; Pirajno, 2009). The presence of quartz, pyrite, anatase, kaolinite, tremolite,
546 barite, and hydrated iron oxides in massively silicified fault-related rocks, suggests precipitation
547 from an acid-sulphate hydrothermal fluid at temperature < 180 °C (Henley and Ellis, 1983; Pirajno,
548 2009; Marchesini et al., 2024). This is consistent with large volumes of fault-related advanced-
549 argillic alteration that are produced by extreme acid leaching with almost complete dissolution of
550 feldspar (Pirajno, 2009; Ece et al., 2013; Hedenquist and Arribas, 2022; Marchesini et al., 2024)
551 (**Figs. 3D, 5B; Table 1**).
552 Since $\delta^{18}O$ values of magmatic fluids typically fall in the range between + 5.5 and + 10 ‰
553 (Taylor, 1979), the obtained mean values for the hydrothermal fluids of -4.9 ‰ SMOW and -1.5
554 ‰ SMOW, calculated from silica and calcite cements, respectively (**Fig. 14D, Table 4**), exclude
555 a predominant magmatic contribution. The negative isotopic composition of these fluids is
556 diagnostic of meteoric-derived fluids heated at depth and it is in accordance with their low salinity

(mean salinity of 1.23 eq. wt% NaCl, Bodnar, 1993). Negative $\delta^{13}C$ values of calcite cements (mean value -3.0 ‰ V-PDB) may suggest interaction with soil and/or vegetation during surficial fluid infiltration (**Fig. 14A**). The δD of the hydrothermal fluids circulating in fault core rocks further suggests their meteoric origin. In fact, δD_w isotopic values for the <2 μm grain-size fractions have generally higher values (average value of -72 ‰; **Table 5**) than those of the whole rock (average value of -94 ‰; **Table 5**), indicating that neoformed clay-minerals (e.g., R3 I-S; **Table 2**) enriching the fine fraction are not in geochemical equilibrium with the minerals inherited from the host rock. These δD_w values are close to the present-day rainfall δD_w values recorded in Greece (between -60‰ and -70‰; Argiriou and Lykoudis, 2006; Lykoudis et al., 2010), thus implying that the neoformed minerals in the <2 μm grain-size fraction are the result of meteoric-derived fluids heated at depth. However, the $\delta^{18}O$ values are slightly heavier than expected for Miocene meteoric fluids at the assumed paleo-latitude ($\delta^{18}O$ = -4.5 ‰ SMOW, Ece et al., 2013), also considering that some of the calculated values from calcite cements fall near 0 ‰ SMOW or considerably above (**Fig. 14**). This enrichment may be attributed to a residual magmatic signature of the fluid or to progressive buffering of ^{18}O-depleted fluids by fluid-rock interaction processes (Bradbury and Woodwell, 1987; Muchez et al., 1995; Lucca et al., 2018; Berio et al., 2022). Various degrees of fluid-rock interaction are supported also by the high content of trace elements in carbonate cements as well as by the similarity of the REE patterns between carbonate cements and volcanic host rocks (**Fig. 15D**). If a reasonable geothermal gradient of 57 °C/km for back-arc/fore-arc settings is assumed (Kolawole and Evenick, 2023), a mean fluid temperature of 160-170 °C implies that meteoric fluid circulation extended to a depth of c. 3 km.

The very similar paleo-temperatures and $\delta^{18}O$ compositions of parental fluids obtained from carbonate and silica cements point to a common fluid source and depth of circulation (**Figs. 13-14**). This hypothesis is further supported by the observed petrographic textures, showing clear cogenetic relations of carbonate and microcrystalline silica in fault-related veins (VS; **Fig. 11D**). This means that the silica-rich fluid was episodically oversaturated with respect to carbonate minerals and that carbonate and silica precipitation can be considered coeval at the time scale of the KAIF activity. If mineral precipitation occurred during boiling, as suggested by mineral textures, calcite precipitation could be triggered by partition into the vapor phase of volatiles such as CO_2 and H_2S that led to a pH increase in the residual fluid (Pirajno, 2009).

Source of Silica

There are several potential silica sources for quartz cementation that, all together, contribute to the overall silica supply, even if some of them are likely to be volumetrically more significant than the others. Weathering and dissolution of feldspars (plagioclase and K-feldspar) are considered an important silica source for silica cementation during sandstone diagenesis in sedimentary basins (McBride, 1989; Worden and Morad, 2009) and for silicification of fault zones in different tectonic contexts and at different P-T conditions, from shallow buried faults to deformation in greenschist conditions (Suh and Dada, 1997; Philit et al., 2015; Verlaguet et al., 2021; Palhano et al., 2023). Particularly, silica in epithermal environments is largely derived by dissolution of feldspars, quartz and volcanic glass (Pirajno, 2009). Verlaguet et al. (2021) noted that silicified fault rocks mainly lack mineral phases able to host alkalis (plagioclase and K-feldspar). Similarly, our data show that, approaching the principal slip surface, silicification promoted a progressive increase in quartz content that is inversely correlated to feldspar content (both plagioclase and K-feldspar; **Fig. 12**). Silicification at the expense of dissolved feldspars by acidic solutions (Fournier, 1985) is also evident from petrographic textures of massively silicified fault-related rocks (**Fig. 8B**). Silica may also result from advanced argillic alteration of the sandstones (**Figs. 3D, 5B, 6A**) because for every mole of K-feldspar altered to kaolinite, two moles of silica are released into the system and are available for silicification (McBride, 1989 and references therein). In addition, silica can result from the smectite to illite conversion, as illite is deficient in silica with respect to smectite. The latter contribution is supported by our X-ray diffraction data showing long-range ordered (R3) mixed layers I-S with an illite content of 90% in fault-related rocks, which suggest an illitization process favored by hydrothermal fluid circulation (**Table 2**).

Moreover, the observed silicification trend in across-fault mineralogical transects with the quartz content that progressively decreases moving away from the principal slip surface (**Fig. 12**) possibly suggests silica precipitation by a migrating fluid that becomes progressively depleted in silica content. Cooling of fluids facilitated silica supersaturation and precipitation, as silica solubility is positively related with temperature (Fournier, 1985; Pirajno, 2009). Consequently, the most plausible scenario is that hydrothermal fluids mineralized the fault zone during their upward migration and cooling. Supersaturation, boiling and conversion of water to steam promoted precipitation of amorphous silica followed by chalcedony and quartz (Fournier, 1985; Pirajno,

2009). However, amorphous silica is more soluble than quartz (Fournier, 1985) and thus more prone to dissolution and re-precipitation.

Structural and Stratigraphic Control on Hydrothermal Alteration and Silicification

The outstanding, continuous exposure of the hydrothermal alterations along the KAIF offers unique insights into the spatial variability and internal mineralogical properties of the hydrothermally altered and silicified zones. Moving along-strike, silicified and brecciated domains vary in size and geometry (**Figs. 5-6**). Silicified and argillic-altered domains are thicker in the northwestern sector of the KAIF, at the fault tip, where a higher structural complexity is documented with several intersecting fault strands (Berio et al., 2023; **Figs. 5B-6A**). This confirms that fault and fracture intersections in areas of high structural complexity (e.g., fault tip) provide volumes of enhanced secondary permeability where the rise of (hydrothermal) fluids and fault-controlled cementation are favored (Eichhubl et al., 2009; Kim and Sanderson, 2010; Person et al., 2012; Peacock et al., 2017). Moving southward, in sectors C and D, silicified, brecciated, and argillic-altered domains progressively fade away (**Fig. 1C**). This is possibly due to the overall evolution of the KAIF system, considering that the E-W segment (sector C) likely developed by breaching the relay zone between the two NW-trending segments, possibly during the late evolutionary history of the fault system and likely after the hydrothermal pulses that had triggered silicification (Berio et al., 2023). This evolutionary scenario would account for a limited along-strike connectivity of the fault system before hard-linkage occurred and, hence, the absence of hydrothermal alteration and silicification in the southeastern sectors.

Moving across-strike, silicified, brecciated, and argillic-altered domains vary in size and geometry (**Figs. 2, 5, 6**). Our across-fault mineralogical transects show that far away from volcanic bodies, the silicification of turbidite sandstones in the footwall damage zone fades into the host rock as one moves away from the principal slip surface (**Fig. 12A, Table 1**). The quartz content in the turbidite sandstones, which can be used as a valuable proxy of the intensity of the silicification process (e.g., Callahan et al., 2020), decreases with increasing distance from the fault core, showing that the intensity of the silicification process correlates inversely with the distance from the fault core (**Fig. 12A**). Accordingly, the boundary between the hydrothermally silicified zone and the host rock is not sharp but, rather, it is a transitional domain characterized by intermediate

mineralogical properties between the two end members. As a consequence, also the petrophysical properties (i.e. matrix porosity and permeability) do not abruptly change, but, instead, they change progressively with increasing distance from the fault core (e.g., Palhano et al., 2023). This mineralogical trend may suggest that the mineralizing fluids, migrating from the fractured inner damage zone (Berio et al., 2023) into the external damage zone, progressively lose their silicification potential possibly because of silica deficiency. Overall, it is worth noting that hydrothermally silicified zones are thicker than the present-day fractured damage zones (Berio et al. 2023) in any structural position along the KAIF. This finding is different from other mineralized extensional fault zones, where the thickness of the domains affected by fault-related diagenesis is systematically smaller than the corresponding damage zones (e.g., Kristensen et al., 2016). This simple geometrical observation suggests that, at least for the studied structural levels, fracture porosity had a limited role in controlling the fault-orthogonal migration of silica-rich fluids responsible for the massive silicification of the turbidite sequence; rather, silicification away from the fault seems to have been predominantly driven by the matrix porosity at the scale of single sandstone layers, i.e. it was controlled by the sedimentary facies. The stratigraphic control on silicification is also well evident at the outcrop-scale, where it is possible to note that porous and permeable sandstone layers, likely acting as collectors for fluids, are more silicified than the clayey mudstone-siltstone intervals (**Fig. 2B**).

Time-Space Evolution of Fault-Related Hydrothermal Alteration and Silicification

Our data allow us to propose a conceptual model in four stages for the time-space evolution of the hydrothermal alteration and silicification along the KAIF. The evolutionary path begins with extensional folding, possibly in a blind fault configuration, followed by fault breakthrough and bedding dip accentuation in both footwall and hanging wall (**Fig. 16A**). Since outcrop-scale observations indicate that silicification postdated the tilting of beds in the footwall block, we can argue that the fault zone was already structured when silicification started and, consequently, an already existing fractured damage zone facilitated fluid ingress, migration, and mineralization (**Fig. 16B**). Consequently, silicification of fault cores and host rocks, and argillic alteration of sandstones by hydrothermal fluids, occurred after a certain amount of displacement had already been accumulated (**Fig. 16B**). Matrix porosity decreased in both the hydrothermally altered fault

cores and damage zones concurrent with hydrothermal alteration and formation of silicified zones (**Fig. 16B**). The formation and growth of these zones limited further fluid migration along and across the fault damage zones, thus potentially allowing fluid pressure to increase (**Fig. 16B**).

After massive silicification and alteration, in the third evolutionary stage, crackle breccias developed in the footwall and vein stockworks in the hanging wall, in otherwise low-porosity and low-permeability, hydrothermally altered and silicified rocks (**Fig. 16C**). These crackle breccias and veins are cemented mostly by silica and carbonate. Given the presence of sharply truncated clasts and fossil fault-related recrystallized silica gels that represent potential markers of seismic faulting (Kirkpatrick et al., 2013; Faber et al., 2014; Fondriest et al., 2015; Smeraglia et al., 2017; Vignaroli et al., 2020; Masoch et al., 2022), the KAIF can be considered an exhumed example of a seismogenic fault (**Fig. 8F**). In this context, crackle breccias and vein stockworks may be interpreted as the product of fluid pressure buildup and hydrofracturing in the pre-seismic stage followed by coseismic rupturing (**Fig. 16C**). Our meso- and micro-structural observations (**Figs. 3C, 8D-E, 9C**) demonstrate that the second and the third stages (**Fig. 16B, C**) were cyclic, implying multiple hydrothermal pulses/cementation events during the seismic cycles. Hydrothermally sealed crackle breccias may have regained cohesive strength between successive slip events (Cox, 2016; Bezerra et al., 2021). Similar breccia textures associated with hydraulic fracturing and multiple stages of silicification and fragmentation were documented along other examples of silicified fault zones (Caine et al., 2010; Bonnemains et al., 2017; Menezes et al., 2019; Cazarin et al., 2021). During the first three stages (**Figs. 16A-C**), the KAIF was characterized by a limited along-strike connectivity with two major hydrologically isolated fault segments that did not allow extensive along-strike fault fluid migration.

During the fourth stage, the KAIF continued to accumulate offset, possibly at shallower burial conditions (**Fig. 16D**). During this final stage, upward hydrothermal fluid migration continued as documented by the mixed layered clay minerals (R3 I-S) of partially-silicified and non-silicified fault core rocks that have an isotopic signature again suggesting a deep circulation of meteoric fluids (**Tables 2 and 5**). Newly formed fractures affected the hydrothermally altered fault-related rocks formed in the previous stages (**Fig. 16D**). The final stage was characterized by widespread iron oxide mineralization of fault cores and of newly formed fractures in the damage zones, whereas silica cementation became subordinate (**Fig. 16D**). During this fourth stage, the

two isolated NW-trending fault segments hard-linked, increasing the along-strike connectivity of the fault system (**Fig. 16D**).

Implications for Porosity and Permeability of Silicified Faults

A common question in oil-and-gas and mining industries is whether fault-related silicification increases or decreases porosity and permeability (Palhano et al., 2023). Based on our results, we briefly explain scenarios where studied hydrothermal products reduce the porosity of pristine rocks and where they increase it within the fault zone, offering insights that could be used as predictive models for industry applications. The massively silicified sandstones within the fault zone have matrix porosity significantly lower than pristine counterparts (**Fig. 7A-B**). Therefore, we suggest that massive silicification tends to reduce fault permeability. However, quartz-cemented crackle breccias developed after bulk silicification generally contain mm- to cm-scale vuggy pores that, if interconnected, enhance fault permeability (**Fig. 3E**). During and after the silicification process, local dissolution of minerals (e.g., feldspars, amorphous and microcrystalline silica, sulfides) within the fault zone may also contribute to the micro-porosity enhancement. Finally, in case of late-stage fault reactivation, the renewed fracturing in the damage zone will be mostly concentrated in the silicified domains of the fault, thus increasing fracture density and connectivity (Berio et al., 2023; Mendes et al., 2024) and consequently increasing fault permeability either vertically and horizontally. Therefore, simple templates are not easy to establish and the time-space evolution of fault-related hydrothermal alterations, their spatial distribution and mineral assemblages should be understood for predictive models.

CONCLUSIONS

The hydrothermally altered, structurally segmented Kornos-Aghios Ioannis Fault was studied by combining field mapping with petrography, mineralogy, geochemistry and fluid inclusion microthermometry of syn-tectonic cements and alteration products. Our multidisciplinary dataset points to the following main conclusions:

1. The Kornos-Aghios Ioannis Fault is locally silicified and altered due to the circulation of hydrothermal fluids. Hydrothermal silicification, alteration, and brecciation are syn-kinematic processes that occurred cyclically during multiple events of fault reactivation.

2. Hydrothermal fluid circulation along the fault produced large volumes of massively silicified and argillic-altered sandstones, locally brecciated and veined, that are heterogeneously distributed across fault strike and may extend up to 250 m in the footwall and 30 m in the hanging wall, with their thickness locally exceeding the damage zone width. Inside the hydrothermally silicified and altered fault zone, quartz-cemented crackle breccias are 70-80 m thick in the footwall block and invariably developed on previously massively silicified and argillic-altered sandstones.
3. Along fault strike, hydrothermal silicification and alteration are strongly heterogeneous at the kilometer-scale. Overall, the northwestern fault segment is strongly affected by hydrothermal silicification and alteration, whereas the central (linking) and southeastern segments are not. This uneven distribution may be controlled by the long-term structural evolution, which started with two hydraulically isolated fault segments that hard-linked after the main silicification process. At a smaller scale (i.e. hundreds of meters), the distribution of fault-related hydrothermal silicification and alteration is controlled by geometric complexities of the fault zone such as breached relay ramps and fault tips, which localize the greatest volumes of silicified, argillic-altered and brecciated rocks. At the meter-scale, silicification is controlled by lithology, being more extensively developed in coarse sandstones than in clayey mudstone-siltstone layers.
4. The hydrothermally silicified and altered fault zone formed by dissolution and precipitation of new mineral phases including amorphous silica phases (frequently recrystallized), microcrystalline silica, quartz, bladed calcite, dolomite, kaolinite, anatase, pyrite, tremolite, barite, long-range ordered mixed I-S layers, and iron oxides/hydroxides. Mineral precipitation was promoted, in the studied porphyry-epithermal environment, by the circulation of acid-sulphate hydrothermal fluids having minimum average temperatures of 160 - 170 °C, ~ 100 °C higher than expected for fluids in thermal equilibrium at maximum burial depth (maximum burial temperature ca 70 °C). The $\delta^{18}O$, the δD, and the low-salinity of mineralizing fluids are diagnostic of a meteoric-derived fluid heated at ~3 km depth (assuming a geothermal gradient of 57 °C/km) and raised along the fault system. The $\delta^{18}O$ signature of the fluid, slightly higher than expected for Miocene meteoric fluids, may also suggest extensive fluid-rock interaction processes or a residual magmatic component.

5. Silica responsible for hydrothermal silicification was sourced by the following processes associated with the circulation of ascending hot fluids along the fault zone: (1) selective feldspar dissolution, (2) advanced-argillic alteration of the sandstones, and (3) smectite to illite conversion.

The study of the hydrothermally altered and silicified Kornos-Aghios Ioannis Fault offers new insights into the interplay between faulting and fluid flow in hydrothermal systems and into the factors controlling the spatial variability and mineralogical/textural properties of fault-related hydrothermal products, with implications upon the permeability structure of silicified faults, fault mineralization and the heterogeneity of sandstone reservoirs.

APPENDIX

Optical Microscopy and Cathodoluminescence

An optical microscopy study was conducted on 98 polished thin sections, by a Zeiss Axioplan 2 microscope and a CITL CL Mk5-2 optical cold cathodoluminescence (CL) apparatus mounted on a Leica DM2700P optical microscope (operating conditions were 250 μA and 10–15 Kv with an exposure time of 10 s), both available at the University of Parma.

Scanning Electron Microscope

Microstructural analysis of fault rocks at the optical microscope was implemented by observations with a Zeiss Gemini 500 FEG-SEM at the Platform of Microscopy of the University of Milano-Bicocca. Thin sections were polished with 1 μm alumina, rinsed in deionized water and then coated with a graphite film of 20 nm in thickness with a Quorum Q150T ES evaporator/sputter. Samples were observed both at SE and BSE working at 15 kV of accelerating voltage, 15 μA of emission current, and 0.2 nA of beam current. The chemical identification of mineralogical phases was carried out with an energy-dispersive A-ray spectrometer (EDS) Bruker Quantax 200EDX.

X-ray Diffraction

X-ray diffraction (XRD) analyses of the whole-rock and the <2 μm grain size fraction of the host rock and partially-silicified to non-silicified fault core rocks were performed on 6 samples using a Bruker D8 Advance X-ray system housed in the X-ray laboratory of the Department of Earth Sciences of Sapienza University of Rome. The instrument was operated at 40 kV and 30 mA using CuKα radiation (λ=1.5406 Å). Randomly oriented whole-rock powders were run in the 2–70 °2θ interval with a step size of 0.02 °2θ and a counting time of 1 s per step while spinning the sample. Oriented air-dried and ethylene-glycol–solvated samples of the <2 μm grain size fraction were scanned from 1 to 48 °2θ and from 1 to 30 °2θ, respectively, with a step size of 0.02 °2θ and a counting time of 2 s per step. The comparison between air-dried and ethylene-glycol solvated patterns allows for the identification of expandable clay minerals such as smectite and mixed layers illite-smectite (I-S). X-ray patterns were collected with variable slit mode to keep the irradiated area on the sample surface constant and converted to fixed slit mode for semiquantitative analysis.

Semi-quantitative estimation of mineral phases was performed by calculating peak areas and using mineral intensity factors as calibration constants (Moore and Reynolds, 1997). Peaks in relatively close position were selected for clay mineral quantitative analysis of the <2 μm fraction in order to minimize the angle-dependent intensity effect. Non-clay minerals that were observed in the <2 μm fraction were not included in the semi-quantitative analysis of the oriented aggregates; thus, data only refer to the phyllosilicate group. The illite content in mixed layer I-S was determined according to Moore and Reynolds (1997) using the delta two-theta method after decomposing the composite peak between 9-10 °2θ and 16-17 °2θ in the ethylene-glycol solvated patterns. The I-S ordering type (Reichweite parameter, R; Jagodzinski 1949) was determined by the position of the I001-S001 reflection between 5 and 8.5 °2θ (Moore and Reynolds 1997). Clay minerals are mainly sensitive to temperature, and the use of mixed layers I-S and the transformation sequence smectite - random - ordered mixed layers I-S (R0) - ordered mixed layers I-S (R1 and R3) - illite-di-octahedral K-mica (muscovite) as indicator of maximum paleotemperature condition is widely accepted (Botti et al., 2004; Corrado et al., 2010; Di Paolo et al., 2012; Izquierdo-Llavall et al., 2013; Schito et al., 2018; Balestra et al., 2019; Aldega et al., 2021). In fact, changes in the composition of mixed layering, layer expandability, and I-S ordering are empirically related to temperature changes due to burial, shear heating or hydrothermal fluids (Hoffman and Hower, 1979; Jennings and Thompson, 1986; Balsamo et al., 2014). Random ordered I-S with illite content lower than 50% indicates early diagenetic conditions at temperature lower than 100°C whereas long-range ordered (R3) I-S indicates deep diagenetic conditions with temperature higher than 160°C (Jennings and Thompson, 1986).

XRD analyses of massively silicified rocks were performed at Parma University on 22 samples by using a Bruker D2 Phaser powder diffractometer (with θ-θ focalizing geometry), which operated at 30 kV and 10 mA with Cu Kα (λ = 1.54178 Å) radiation. Specimens were run in the 5-80° 2θ range, with a step size of 0.018 °2θ and a counting time of 1 s per step while spinning the sample. Qualitative analysis of major crystalline phases was performed using the EVA identification software and the Crystallography Open Database (COD). Rietveld refinements were performed by GSAS and EXPGUI packages (Toby and Von Dreele, 2013) to quantify the crystalline phases and adding a 10 wt.% high purity Si as a reference standard. Single phase scale factors, cell parameters and peaks profile coefficients for each phase were refined as well as the instrumental zero. Background was also refined, using a 10 terms Chebychev polynomial. The

quantitative results are reported and as the RIR-Rietveld results normalized to 100 wt. %. For the massively silicified rocks, the mineralogical assemblage of the <2 µm fraction was not determined due to the very low amount of material that we were able to extract.

Laser Ablation Inductively Coupled Mass Spectrometry (LA-ICP-MS)

Five 100 µm-thick sections were analyzed for major and trace elements (a total of 47 analyses were performed) of calcite and dolomite cements in veins by *in situ* LA-ICP-MS using a 213 nm laser ablation system coupled to an iCAP TQ ICP MS (Thermo Scientific), housed at Centro Interdipartimentale Grandi Strumenti (CIGS) of the University of Modena and Reggio-Emilia. The system was tuned for maximum sensitivity on NIST612, while keeping low-oxide levels in the plasma (ThO/Th < 1%). Elemental data were acquired using a laser spot size of 80 µm, a frequency of 10 Hz, a fluence of 6 J cm^{-2} and a He flux of 0.6 l min^{-1} (see Giovanardi et al., 2018; Cipriani et al., 2023). Before the *in situ* analysis, the surface of the sample was carefully pre-ablated to remove possible contaminants. Several spot analyses were collected for each sample (the sampling sites of *in situ* analysis are shown in **Figs. S1-S5** in the Supplemental Material[1]). The following masses were measured: ^{24}Mg, ^{55}Mn, ^{57}Fe, ^{88}Sr, ^{89}Y, ^{139}La, ^{140}Ce, ^{141}Pr, ^{146}Nd, ^{147}Sm, ^{153}Eu, ^{157}Gd, ^{159}Tb, ^{163}Dy, ^{165}Ho, ^{166}Er, ^{169}Tm, ^{172}Yb, ^{175}Lu, for a total sweep time of ~0.7 s. Raw ICP counts were normalized using ^{43}Ca as internal standard and NIST612 as external reference material (Jochum et al. 2005), using an in-house R script. Relative standard deviation (RSD) was better than 10%. Eu and Ce anomalies have been calculated using the equation of Debruyne et al. (2016). The complete data set is reported in the Supplemental Material[1], **Table S2** and **Table S3**.

Stable Isotope Analyses

Oxygen and Carbon

A handheld dental drill was used to extract 25 powdered samples from fresh section cuts of host rock, veins and fault rock. Powdered samples of silica cements were treated with diluted HCl to remove any carbonate and then rinsed five times with MilliQ water.

Stable isotope analyses (oxygen) of silica cements were carried out at the Stable Isotope Laboratory of GNS Science located at the National Isotope Centre (NIC), Gracefield, Wellington, New Zealand. Oxygen was extracted from sample powders using a CO_2-laser and BrF_5 fluorination

879 technique (Sharp, 1990). Samples were normalized to the international quartz standard NBS-28
880 using a value of +9.6 per mil (‰). Values for four NBS-28 analyzed with the samples had 1σ
881 standard deviation of 0.11 ‰. Samples and standards were heated overnight to 200 °C prior to
882 loading into the vacuum extraction line. These were then evacuated for approximately 12 hours
883 prior to extraction. Blank BrF_5 runs were done until yield was less than 0.2 μmoles oxygen.
884 Oxygen yields were recorded, and CO_2 gas was analyzed on a GVI Isoprime mass spectrometer.
885 Oxygen isotope values are reported in SMOW.
886 Oxygen and carbon analyses of carbonate cements were carried out at Parma University with
887 a Thermo Finnigan DELTA Plus XP mass spectrometer coupled with a Thermo Finnigan
888 GasBench II gas preparation and introduction system. $\delta^{18}O$ and $\delta^{13}C$ are reported in the
889 conventional delta notation with respect to the international standard V-PDB. Measurement
890 reproducibility was 0.15‰ for $\delta^{13}C$ and c. 0.20‰ for $\delta^{18}O$.
891 The complete dataset is reported in the Supplemental Material[1], **Table S4** and **Table S5**.
892
893 *Hydrogen*
894 Hydrogen stable isotopes were measured on 7 samples for both whole rock and <2 μm
895 grain size fractions of host rocks and partially silicified to non-silicified fault core rocks. The
896 technique for producing H_2 involves the reduction of samples by pyrolysis reaction with glassy
897 carbon in a high-T reaction furnace at 1450 °C (Brand et al., 1994) with a He carrier gas, following
898 the method described by Sharp et al. (2001). An aliquot of 1-2 mg of sample is wrapped in silver
899 foil capsules and dropped into the furnace by an autosampler. The product gas is separated in a gas
900 chromatograph and analyzed in a mass spectrometer configured to measure H-isotope in
901 continuous flow mode. Every sample is analyzed two or more times, and the D/H ratios are
902 corrected using a standard linear regression procedure. The used standards for the analysis,
903 repeated every series of six samples, are Bonsall, LR151, and NBS30 biotite, and LR8 amphibole.
904 The analyses were performed with a Thermo-Fisher high-T analyzer (Flash-HT), linked to a
905 Thermo-Fisher Delta V IRMS via a Conflo IV interface, housed in the stable isotope laboratory at
906 the Department of Earth Sciences of Sapienza University (Rome). Hydrogen stable isotope results
907 are presented in the standard delta notation SMOW δD (‰). The δD values from rock samples and
908 <2 μm grain size fraction were averaged and then converted to δDw values of water, by calculating
909 the weight percent of each H-bearing mineral as quantified by XRD ($\frac{wt_m\%}{100}$) and using their

respective mineral-water fractionation factors (α). The formula is $\delta Dw = \left[\frac{1000+\delta D}{\alpha} - 1000\right] \times \frac{wt\%}{100}$, based on Suzuoki and Epstein (1976) and Yeh (1980). The α are taken from Graham et al. (1987), Capuano (1992), Vennemann and O'Neil (1996) and Hyeong and Capuano (2004).

Fluid Inclusions Microthermometry

Fluid inclusions were studied in quartz and calcite on 5 thick (100–130 μm) doubly polished rock wafers. Fluid inclusions were studied in fluid inclusion assemblages (FIAs; e.g., Goldstein and Reynolds 1994). Wafers were broken into smaller pieces to collect microthermometry data. Fluid inclusion microthermometry was performed at Parma University using a Linkam THMSG-600 heating–cooling stage coupled with a Leica DM 2500 microscope. The stage was calibrated by synthetic Syn Flinc™ fluid inclusion standards. Two-phase aqueous inclusions were initially heated to avoid their artificial stretching during freezing. In two-phase inclusions, only homogenization temperatures (Th) and melting temperatures of ice and clathrates ($Tm_{ice/cla}$) were measured because first melting temperatures were not recognizable. Homogenization temperatures (Th) are minimum values at which fluids could have been trapped, and no corrections were made for pressure effects on temperature (Goldstein and Reynolds 1994).

The complete dataset is reported in the Supplemental Material[1], **Table S6**.

ACKNOWLEDGMENTS

The authors thankfully acknowledge Francisco Hilario Bezerra, Peter Eichhubl and the Associate Editor Marcin Dabrowski whose criticisms helped to substantially improve the paper. The authors wish to thank Andrea Comelli for thin section preparation. Enrico Maria Selmo and Kevin Faure are acknowledged for stable isotope analysis. The authors acknowledge financial support by the Italian Ministry of University, and Research (MUR) through PRIN project "FAST- Fault architecture in space and time" (PRIN 2020, PI G. Viola, local coordinator F. Balsamo; CUP J33C22000170001). This work has benefited from the equipment and framework of the "COMP-HUB" and "COMP-R" Initiatives, funded by the "Departments of Excellence" program of the Italian Ministry for University and Research (MIUR, 2018–2022 and MUR, 2023–2027).

REFERENCES CITED

Aldega, L., Carminati, E., Scharf, A., and Mattern, F., 2021, Thermal maturity of the Hawasina units and origin of the Batinah Mélange (Oman Mountains): Insights from clay minerals: Marine and Petroleum Geology, v. 133, p. 105316, doi:10.1016/j.marpetgeo.2021.105316.

Anifadi, A., Parcharidis, I., and Sykioti, O., 2017, Hydrothermal Alteration Zones Detection in Limnos Island, Through the Application of Remote Sensing: Bulletin of the Geological Society of Greece, v. 50, p. 1595–1604, doi:10.12681/bgsg.11879.

Argiriou, A.A., and Lykoudis, S., 2006, Isotopic composition of precipitation in Greece: Journal of Hydrology, v. 327, p. 486–495, doi:10.1016/j.jhydrol.2005.11.053.

Armijo, R., Meyer, B., Hubert, A., and Barka, A., 1999, Westward propagation of the North Anatolian fault into the northern Aegean: Timing and kinematics: Geology, v. 27, p. 267–270, doi:10.1130/0091-7613(1999)027<0267:WPOTNA>2.3.CO;2.

Balestra, M., Corrado, S., Aldega, L., Morticelli, M.G., Sulli, A., Rudkiewicz, J.L., and Sassi, W., 2019, Thermal and structural modeling of the Scillato wedge-top basin source-to-sink system: Insights into the Sicilian fold-and-thrust belt evolution (Italy): Bulletin of the Geological Society of America, v. 131, p. 1763–1782, doi:10.1130/B35078.1.

Balsamo, F., Aldega, L., De Paola, N., Faoro, I., and Storti, F., 2014, The signature and mechanics of earthquake ruptures along shallow creeping faults in poorly lithified sediments: Geology, v. 42, p. 435–438, doi:10.1130/G35272.1.

Berio, L.R., Balsamo, F., Pizzati, M., Storti, F., Curzi, M., and Viola, G., 2023, Along- and across-strike variation of damage zone parameters in the Kornos-Aghios Ioannis normal fault, Lemnos Island, Greece: Journal of Structural Geology, v. 177, p. 104981, doi:10.1016/j.jsg.2023.104981.

964 Berio, L.R., Mittempergher, S., Storti, F., Bernasconi, S.M., Cipriani, A., Lugli, F., and Balsamo,
965 F., 2022, Open – closed – open palaeofluid system conditions recorded in the tectonic vein
966 networks of the Parmelan anticline (Bornes Massif, France): Journal of the Geological
967 Society, v. 179, p. jgs2021-117.
968 Bezerra, F.H., Balsamo, F., Corsi, G., Michel, J., Maria, O., Sousa, L., Nogueira, F.C.C., Salvioli-
969 Mariani, E., and Menezes, C.P., 2021, Hydrothermal silicification in the intraplate
970 Samambaia seismogenic fault, Brazil: Implications for fault loss of cohesion and healing in
971 rifted crust: Tectonophysics, v. 815, p. 229002, doi:10.1016/j.tecto.2021.229002.
972 Bodnar, R.J., 1993, Revised equation and table for determining the freezing point depression of
973 H2O-NaCl solutions: Geochimica et Cosmochimica Acta, v. 57, p. 683–684,
974 doi:10.1016/0016-7037(93)90378-A.
975 Boles, J.R., Eichhubl, P., Garven, G., and Chen, J., 2004, Evolution of a hydrocarbon migration
976 pathway along basin-bounding faults: evidence from fault cement: AAPG Bulletin, v. 88, p.
977 971–990.
978 Bonev, N., and Beccaletto, L., 2007, From syn- to post-orogenic Tertiary extension in the north
979 Aegean region: Constraints on the kinematics in the eastern Rhodope-Thrace, Bulgaria-
980 Greece and the Biga Peninsula, NW Turkey: Geological Society Special Publication, v. 291,
981 p. 113–142, doi:10.1144/SP291.6.
982 Bonnemains, D., Escartín, J., Mével, C., Andreani, M., and Verlaguet, A., 2017, Pervasive
983 silicification and hanging wall overplating along the 138200N oceanic detachment fault (Mid-
984 Atlantic Ridge): Geochemistry Geophysics Geosystems, v. 18, p. 2028–2053,
985 doi:10.1002/2017GC006846.
986 Börner, F., Keith, M., Bücker, J.L., Voudouris, P., Klemd, R., Haase, K., Kutzschbach, M., and

Schiperski, F., 2022, In-situ trace element and S isotope systematics in pyrite from three porphyry-epithermal prospects, Limnos Island, Greece: Frontiers in Earth Science, v. 10, p. 916107, doi:10.3389/feart.2022.916107.

Botti, F., Aldega, L., and Corrado, S., 2004, Sedimentary and tectonic burial evolution of the Northern Apennines in the Modena-Bologna area: Constraints from combined stratigraphic, structural, organic matter and clay mineral data of Neogene thrust-top basins: Geodinamica Acta, v. 17, p. 185–203, doi:10.3166/ga.17.185-203.

Bradbury, H.J., and Woodwell, G.R., 1987, Ancient fluid flow within foreland terrains: Geological Society Special Publication, v. 34, p. 87–102, doi:10.1144/GSL.SP.1987.034.01.07.

Brand, W.A., Tegtmeyer, A.R., and Hilkert, A., 1994, Compound-specific isotope analysis: extending toward 15N14N and 18O16O: Organic Geochemistry, v. 21, p. 585–594, doi:10.1016/0146-6380(94)90004-3.

Caine, J.S., Bruhn, R.L., and Forster, C.B., 2010, Internal structure, fault rocks, and inferences regarding deformation, fluid flow, and mineralization in the seismogenic Stillwater normal fault, Dixie Valley, Nevada: Journal of Structural Geology, v. 32, p. 1576–1589, doi:10.1016/j.jsg.2010.03.004.

Callahan, O.A., Eichhubl, P., and Davatzes, N.C., 2020, Mineral precipitation as a mechanism of fault core growth: Journal of Structural Geology, v. 140, p. 104156, doi:10.1016/j.jsg.2020.104156.

Callahan, O.A., Eichhubl, P., Olson, J.E., and Davatzes, N.C., 2019, Fracture Mechanical Properties of Damaged and Hydrothermally Altered Rocks, Dixie Valley-Stillwater Fault Zone, Nevada, USA: Journal of Geophysical Research: Solid Earth, v. 124, p. 4069–4090, doi:10.1029/2018JB016708.

1010 Capuano, R.M., 1992, The temperature dependence of hydrogen isotope fractionation between
1011 clay minerals and water: Evidence from a geopressured system: Geochimica et
1012 Cosmochimica Acta, v. 56, p. 2547–2554, doi:10.1016/0016-7037(92)90208-Z.
1013 Caputo, R., Chatzipetros, A., Pavlides, S., and Sboras, S., 2012, The greek database of seismogenic
1014 sources (GreDaSS): State-of-the-art for northern greece: Annals of Geophysics, v. 55, p. 859–
1015 894, doi:10.4401/ag-5168.
1016 Caracciolo, L., Critelli, S., Innocenti, F., Kolios, N., and Manetti, P., 2011, Unravelling provenance
1017 from Eocene-Oligocene sandstones of the Thrace Basin, North-east Greece: Sedimentology,
1018 v. 58, p. 1988–2011, doi:10.1111/j.1365-3091.2011.01248.x.
1019 Cazarin, C.L. et al., 2021, Hydrothermal activity along a strike-slip fault zone and host units in the
1020 São Francisco Craton, Brazil – Implications for fluid flow in sedimentary basins: Precambrian
1021 Research, v. 365, p. 106365, doi:10.1016/j.precamres.2021.106365.
1022 Cerchiari, A., Remitti, F., Mittempergher, S., Festa, A., Lugli, F., and Cipriani, A., 2020, Cyclical
1023 variations of fluid sources and stress state in a shallow megathrust-zone mélange: Journal of
1024 the Geological Society, v. 177, p. 647–659, doi:10.1144/jgs2019-072.
1025 Cipriani, A., Giovanardi, T., Mazzucchelli, M., Lugli, F., Sforna, M.C., Gualtieri, A.F., Di
1026 Giuseppe, D., Gaeta, M., and Brunelli, D., 2023, Origin of a carbonate-bearing fluorapatite
1027 from Tertiary volcanics of the Veneto Volcanic Province, Italy: Mineralogy and Petrology,
1028 v. 117, p. 573–594, doi:10.1007/s00710-023-00831-4.
1029 Clayton, R.N., O'Neil, J.R., and Mayeda, T.K., 1972, Oxygen isotope exchange between quartz
1030 and water: Journal of Geophysical Research, v. 77, p. 3057–3067,
1031 doi:10.1029/jb077i017p03057.
1032 Corrado, S., Aldega, L., and Zattin, M., 2010, Sedimentary vs. tectonic burial and exhumation

along the Apennines (Italy): Journal of the Virtual Explorer, v. 36, doi:10.3809/jvirtex.2009.00232.

Cox, S.F., 2016, Injection-driven swarm seismicity and permeability enhancement: Implications for the dynamics of hydrothermal ore systems in high fluid-flux, overpressured faulting regimes - An invited paper: Economic Geology, v. 111, p. 559–587, doi:10.2113/econgeo.111.3.559.

Curzi, M., Aldega, L., Billi, A., Boschi, C., Carminati, G., Vignaroli, G., and Bernasconi, S.M., 2024, Fossilchemical-physical (dis)equilibria between paleofluids and host rocks and their relationship to the seismiccycle and earthquakes: Earth Science Reviews, p. 101865, doi:https://doi.org/10.1016/j.earscirev.2024.104801(in press).

Davies, G.R., and Smith, L.B., 2006, Structurally controlled hydrothermal dolomite reservoir facies: An overview: AAPG Bulletin, v. 11, p. 1641–1690, doi:10.1306/05220605164.

Dong, G., Morrison, G., and Jaireth, S., 1995, Quartz textures in epithermal veins, Queensland - classification, origin, and implication: Economic Geology, v. 90, p. 1841–1856, doi:10.2113/gsecongeo.90.6.1841.

Ece, Ö.I., Ekinci, B., Schroeder, P.A., Crowe, D., and Esenli, F., 2013, Origin of the Düvertepe kaolin-alunite deposits in Simav Graben, Turkey: Timing and styles of hydrothermal mineralization: Journal of Volcanology and Geothermal Research, v. 255, p. 57–78, doi:10.1016/j.jvolgeores.2013.01.012.

Eichhubl, P., and Boles, J.R., 2000, Rates of fluid flow in fault systems - Evidence for Episodic Fluid Flow in the Miocene Monterey Formation, Coastal California: American Journal of Science, v. 300, p. 571–600.

Eichhubl, P., Davatzes, N.C., and Becker, S.P., 2009, Structural and diagenetic control of fluid

migration and cementation along the Moab fault, Utah: AAPG Bulletin, v. 93, p. 653–681, doi:10.1306/02180908080.

Essarraj, S., Boiron, M.C., Cathelineau, M., and Fourcade, S., 2001, Multistage deformation of Au-quartz veins (Laurieras, French Massif Central): Evidence for late gold introduction from microstructural, isotopic and fluid inclusion studies: Tectonophysics, v. 336, p. 79–99, doi:10.1016/S0040-1951(01)00095-6.

Faber, C., Rowe, C.D., Miller, J.A., Fagereng, Å., and Neethling, J.H., 2014, Silica gel in a fault slip surface: Field evidence for palaeo-earthquakes? Journal of Structural Geology, v. 69, p. 108–121, doi:10.1016/j.jsg.2014.09.021.

Faulkner, D.R., Jackson, C.A.L., Lunn, R.J., Schlische, R.W., Shipton, Z.K., Wibberley, C.A.J., and Withjack, M.O., 2010, A review of recent developments concerning the structure, mechanics and fluid flow properties of fault zones: Journal of Structural Geology, v. 32, p. 1557–1575, doi:10.1016/j.jsg.2010.06.009.

Fernandez-Ibanez, F., Nolting, A., Breithaupt, C.I., Darby, B., Mimoun, J., and Henares, S., 2022, The properties of faults in the Brazil pre-salt: A reservoir characterization perspective: Marine and Petroleum Geology, v. 146, p. 105955, doi:10.1016/j.marpetgeo.2022.105955.

Fondriest, M., Aretusini, S., Di Toro, G., and Smith, S.A.F., 2015, Fracturing and rock pulverization along an exhumed seismogenic fault zone in dolostones: The Foiana Fault Zone (Southern Alps, Italy): Tectonophysics, v. 654, p. 56–74, doi:10.1016/j.tecto.2015.04.015.

Fornadel, A.P., Voudouris, P.C., Spry, P.G., and Melfos, V., 2012, Mineralogical, stable isotope, and fluid inclusion studies of spatially related porphyry Cu and epithermal Au-Te mineralization, Fakos Peninsula, Limnos Island, Greece: Mineralogy and Petrology, v. 105, p. 85–111, doi:10.1007/s00710-012-0196-8.

1079 Fournier, R.O., 1985, The behavior of silica in hydrothermal solutions, *in* Berger, B.R., Bethke,
1080 P.M., (eds.), Geology and Geochemistry of Epithermal Systems. Reviews in Economic
1081 Geology, Volume 2, p. 45–61, doi:https://doi.org/10.5382/Rev.02.
1082 Giovanardi, T., Mazzucchelli, M., Lugli, F., Girardi, V.A.V., Correia, C.T., Tassinari, C.C.G., and
1083 Cipriani, A., 2018, Isotopic constraints on contamination processes in the Tonian Goiás
1084 Stratiform Complex: Lithos, v. 310–311, p. 136–152, doi:10.1016/j.lithos.2018.04.008.
1085 Goldstein, R., & Reynolds, J. (1994). Systematics of fluid inclusions. *SEPM short course*
1086 *notes*, *31*, 188.
1087 Graham, C.M., Viglino, J.A., and Harmon, R.S., 1987, Experimental study of hydrogen-isotope
1088 exchange between aluminous chlorite and water and of hydrogen diffusion in chlorite:
1089 American Mineralogist, v. 72, p. 566–579.
1090 Grare, A., Lacombe, O., Mercadier, J., Benedicto, A., Guilcher, M., Trave, A., Ledru, P., and
1091 Robbins, J., 2018, Fault zone evolution and development of a structural and hydrological
1092 barrier: The quartz breccia in the Kiggavik area (Nunavut, Canada) and its control on uranium
1093 mineralization: Minerals, v. 8, p. 1–28, doi:10.3390/min8080319.
1094 Guillou-Frottier, L., Milesi, G., Roche, V., Duwiquet, H., and Taillefer, A., 2024, Heat flow,
1095 thermal anomalies, tectonic regimes and high-temperature geothermal systems in fault zones:
1096 Comptes Rendus - Geoscience, v. 356, p. 389–421, doi:https://doi.org/10.5802/crgeos.213
1097 Geodynamics.
1098 Gülyüz, N., Kuşcu, I., and Shipton, Z.K., 2023, Multiphase deformation, fluid flow and
1099 mineralization in epithermal systems: Inferences from structures, vein textures and breccias
1100 of the Kestanelik epithermal Au-Ag deposit, NW Turkey: Turkish Journal of Earth Sciences,
1101 v. 32, p. 75–95, doi:10.55730/1300-0985.1828.

1102 Hedenquist, J.W., and Arribas, A., 2022, Exploration Implications of Multiple Formation
1103 Environments of Advanced Argillic Minerals: Economic Geology, v. 117, p. 609–643,
1104 doi:10.5382/econgeo.4880.
1105 Henley, R.W., and Ellis, A.J., 1983, Geothermal Systems Ancient and Modern: A Geochemical
1106 Review: Earth-Science Reviews, v. 19, p. 1–50, doi:https://doi.org/10.1016/0012-
1107 8252(83)90075-2.
1108 Hoffman, J., and Hower, J., 1979, Clay Mineral Assemblages As Low Grade Metamorphic
1109 Geothermometers: Application To the Thrust Faulted Disturbed Belt of Montana, U.S.A.:
1110 Aspects of Diagenesis: SEMP Special Publication, v. 26, p. 55–79,
1111 doi:10.2110/pec.79.26.0055.
1112 Hyeong, K., and Capuano, R.M., 2004, Hydrogen isotope fractionation factor for mixed-layer
1113 illite/smectite at 60° to 150°C: New data from the northeast Texas Gulf Coast: Geochimica
1114 et Cosmochimica Acta, v. 68, p. 1529–1543, doi:10.1016/j.gca.2003.10.002.
1115 Innocenti, F., Manetti, P., Mazzuoli, R., Pertusati, P., Fytikas, M., and Kolios, N., 1994, The
1116 geology and geodynamic significance of the Island of Limnos, North Aegean Sea, Greece:
1117 Neues Jahrbuch für Geologie und Paläontologie, v. 11, p. 661–691,
1118 doi:10.1127/njgpm/1994/1994/661.
1119 Innocenti, F., Manetti, P., Mazzuoli, R., Pertusati, P., Fytikas, M., Kolios, N., Vougioukalakis,
1120 G.E., Androulakakis, N., Critelli, S., and Caracciolo, L., 2009, Geological Map (Scale
1121 1:50,000) of Limnos Island (Greece) : Explanatory Notes: Acta Vulcanologica, v. 21, p. 123–
1122 134, doi:10.1400/146017.
1123 Izquierdo-Llavall, E., Aldega, L., Cantarelli, V., Corrado, S., Gil-Peña, I., Invernizzi, C., and
1124 Casas, A.M., 2013, On the origin of cleavage in the Central Pyrenees: Structural and paleo-

thermal study: Tectonophysics, v. 608, p. 303–318, doi:10.1016/j.tecto.2013.09.027.

Jagodzinski, H., 1949. Eindimensionale Fehlordnung in Kristallen und ihr Einfluss auf die Röntgen Interferenzen. Acta Cryst., v. 2, p. 201-207.

Jébrak, M., 1997, Hydrothermal breccias in vein-type ore deposits: A review of mechanisms, morphology and size distribution: Ore Geology Reviews, v. 12, p. 111–134, doi:10.1016/S0169-1368(97)00009-7.

Jennings, S., and Thompson, G.R., 1986, Diagenesis of Plio-Pleistocene Sediments of the Colorado River Delta, Southern California: Journal of Sedimentary Petrology, v. 56, p. 89–98, doi:10.1306/212F8891-2B24-11D7-8648000102C1865D.

de Jesus, I.L., Abrantes, F.R., Ariza Ferreira, D.J., and Lupinacci, W.M., 2023, Carbonate reservoir quality and permoporosity obliteration due to silicification processes in the Barra Velha Formation, Santos Basin, Southeastern Brazil: Brazilian Journal of Geology, v. 53, p. 1–17, doi:10.1590/2317-4889202320220086.

Jolivet, L. et al., 2013, Aegean tectonics: Strain localisation, slab tearing and trench retreat: Tectonophysics, v. 597–598, p. 1–33, doi:10.1016/j.tecto.2012.06.011.

Jolivet, L., and Brun, J.P., 2010, Cenozoic geodynamic evolution of the Aegean: International Journal of Earth Sciences, v. 99, p. 109–138, doi:10.1007/s00531-008-0366-4.

Jolivet, L., Brun, J.-P., Gautier, P., Lallemant, S., and Patriat, M., 1994, 3D-kinematics of extension in the Aegean region from the early Miocene to the Present, insights from the ductile crust: Bulletin de la Societe Geologique de France, v. 165, p. 195–209.

Jolivet, L., Menant, A., Clerc, C., Sternai, P., Bellahsen, N., Leroy, S., Pik, R., Stab, M., Faccenna, C., and Gorini, C., 2018, Extensional crustal tectonics and crust-mantle coupling, a view from the geological record: Earth-Science Reviews, v. 185, p. 1187–1209,

doi:10.1016/j.earscirev.2018.09.010.

Jones, B., and Renaut, R.W., 1998, Origin of platy calcite crystals in hot-spring deposits in the Kenya Rift Valley: Journal of Sedimentary Research, v. 68, p. 913–927, doi:https://doi.org/10.2110/jsr.68.913.

Kim, Y.S., and Sanderson, D.J., 2010, Inferred fluid flow through fault damage zones based on the observation of stalactites in carbonate caves: Journal of Structural Geology, v. 32, p. 1305–1316, doi:10.1016/j.jsg.2009.04.017.

Kiratzi, A.A., and Svigkas, N., 2013, A study of the 8 January 2013 Mw5.8 earthquake sequence (Lemnos Island, East Aegean Sea): Tectonophysics, v. 608, p. 452–460, doi:10.1016/j.tecto.2013.09.002.

Kirkpatrick, J.D., Rowe, C.D., White, J.C., and Brodsky, E.E., 2013, Silica gel formation during fault slip: Evidence from the rock record: Geology, v. 41, p. 1015–1018, doi:10.1130/G34483.1.

Kirschner, D.L., Masson, H., and Sharp, Z.D., 1999, Fluid migration through thrust faults in the Helvetic nappes (Western Swiss Alps): Contributions to Mineralogy and Petrology, v. 136, p. 169–183, doi:10.1007/s004100050530.

Kolawole, F., and Evenick, J.C., 2023, Global distribution of geothermal gradients in sedimentary basins: Geoscience Frontiers, v. 14, p. 101685, doi:10.1016/j.gsf.2023.101685.

Koukouvelas, I.K., and Aydin, A., 2002, Fault structure and related basins of the North Aegean Sea and its surroundings: Tectonics, v. 21, p. 10–17, doi:10.1029/2001TC901037.

Kristensen, T.B., Rotevatn, A., Peacock, D.C.P., Henstra, G.A., Midtkandal, I., and Grundvåg, S., 2016, Structure and flow properties of syn-rift border faults: The interplay between fault damage and fault-related chemical alteration: Journal of Structural Geology, v. 92, p. 99–115,

doi:10.1016/j.jsg.2016.09.012.

Labaume, P., and Moretti, I., 2001, Diagenesis-dependence of cataclastic thrust fault zone sealing in sandstones. Example from the Bolivian Sub-Andean Zone: Journal of Structural Geology, v. 23, p. 1659–1675, doi:10.1016/S0191-8141(01)00024-4.

Lacroix, B., Travé, A., Buatier, M., Labaume, P., Vennemann, T., and Dubois, M., 2014, Syntectonic fluid-flow along thrust faults: Example of the South-Pyrenean fold-and-thrust belt: Marine and Petroleum Geology, v. 49, p. 84–98, doi:10.1016/j.marpetgeo.2013.09.005.

Laubach, S.E., Eichhubl, P., Hargrove, P., Ellis, M.A., and Hooker, J.N., 2014, Fault core and damage zone fracture attributes vary along strike owing to interaction of fracture growth, quartz accumulation, and differing sandstone composition: Journal of Structural Geology, v. 68, p. 207–226, doi:10.1016/j.jsg.2014.08.007.

Lima, B.E.M., Tedeschi, L.R., Pestilho, A.L.S., Santos, R.V., Vazquez, J.C., Guzzo, J.V.P., and De Ros, L.F., 2020, Deep-burial hydrothermal alteration of the Pre-Salt carbonate reservoirs from northern Campos Basin, offshore Brazil: Evidence from petrography, fluid inclusions, Sr, C and O isotopes: Marine and Petroleum Geology, v. 113, p. 104143, doi:10.1016/j.marpetgeo.2019.104143.

Liotta, D. et al., 2023, Tectonic-magmatic-hydrothermal interactions in a hot dry rock geothermal system: The role of the transfer and normal faults in the Acoculco caldera (Mexico): Journal of Volcanology and Geothermal Research, v. 444, p. 107963, doi:10.1016/j.jvolgeores.2023.107963.

Liotta, D., Brogi, A., Ruggieri, G., and Zucchi, M., 2021, Fossil vs. active geothermal systems: A field and laboratory method to disclose the relationships between geothermal fluid flow and geological structures at depth: Energies, v. 14, p. 933, doi:10.3390/en14040933.

Lucca, A., Storti, F., Molli, G., Muchez, P., Schito, A., Artoni, A., Balsamo, F., Corrado, S., and Salvioli-Mariani, E., 2018, Seismically enhanced hydrothermal plume advection through the process zone of the Compione extensional Fault, Northern Apennines, Italy: GSA Bulletin, v. 131, p. 547–571, doi:10.1130/b32029.1.

Lykoudis, S.P., Kostopoulou, E., and Argiriou, A.A., 2010, Stable isotopic signature of precipitation under various synoptic classifications: Physics and Chemistry of the Earth, v. 35, p. 530–535, doi:10.1016/j.pce.2009.09.002.

Machel, H.G., and Lonnee, J., 2002, Hydrothermal dolomite - A product of poor definition and imagination: Sedimentary Geology, v. 152, p. 163–171, doi:10.1016/S0037-0738(02)00259-2.

Maravelis, A.G., Boutelier, D., Catuneanu, O., Seymour, K.S., and Zelilidis, A., 2016, A review of tectonics and sedimentation in a forearc setting: Hellenic Thrace Basin, North Aegean Sea and Northern Greece: Tectonophysics, v. 674, p. 1–19, doi:10.1016/j.tecto.2016.02.003.

Maravelis, A.G., Pantopoulos, G., Tserolas, P., and Zelilidis, A., 2015, Accretionary prism–forearc interactions as reflected in the sedimentary fill of southern Thrace Basin (Lemnos Island, NE Greece): International Journal of Earth Sciences, v. 104, p. 1039–1060, doi:10.1007/s00531-014-1130-6.

Marchesini, B., Tavani, S., Mercuri, M., Mondillo, N., Pizzati, M., Balsamo, F., Aldega, L., and Carminati, E., 2024, Structural control on the alteration and fluid flow in the lithocap of the Allumiere-Tolfa epithermal system: Journal of Structural Geology, v. 179, p. 105035, doi:10.1016/j.jsg.2023.105035.

Masoch, S., Fondriest, M., Gomila, R., Jensen, E., Mitchell, T.M., Cembrano, J., Pennacchioni, G., and Di Toro, G., 2022, Along-strike architectural variability of an exhumed crustal-scale

seismogenic fault (Bolfin Fault Zone, Atacama Fault System, Chile): Journal of Structural Geology, v. 165, p. 104745, doi:10.1016/j.jsg.2022.104745.

Mazzarini, F., Musumeci, G., Viola, G., Garofalo, P.S., and Mattila, J., 2019, Structural and lithological control on fluid circulation, dilation and ore mineralization (Rio Albano mine, Island of Elba, Italy): Journal of Structural Geology, v. 126, p. 210–230, doi:10.1016/j.jsg.2019.06.012.

McBride, E.F., 1989, Quartz cement in sandstones: a review: Earth Science Reviews, v. 26, p. 69–112, doi:10.1016/0012-8252(89)90019-6.

McDonough, W.F., and Sun, S. s., 1995, The composition of the Earth: Chemical Geology, v. 120, p. 223–253, doi:10.1016/0009-2541(94)00140-4.

Mendes, L. de C. et al., 2024, The influence of major faults and fractures on the development of non-matrix porosity system in a pre-salt carbonate reservoir, Santos Basin – Brazil: Journal of Structural Geology, v. 189, p. 105271, doi:10.1016/j.jsg.2024.105271.

Menezes, C.P., Bezerra, F.H.R., Balsamo, F., Mozafari, M., Vieira, M.M., Srivastava, N.K., and de Castro, D.L., 2019, Hydrothermal silicification along faults affecting carbonate-sandstone units and its impact on reservoir quality, Potiguar Basin, Brazil: Marine and Petroleum Geology, v. 110, p. 198–217, doi:10.1016/j.marpetgeo.2019.07.018.

Moore, D.M., Reynolds, R.C. Jr., 1997. X-Ray Diffraction and the identification and analysis of clay minerals. Oxford University Press, Oxford, UK, 378 pp.

Mozafari, M., Swennen, R., Balsamo, F., El Desouky, H., Storti, F., and Taberner, C., 2019, Fault-controlled dolomitization in the Montagna dei Fiori Anticline (Central Apennines, Italy): Record of a dominantly pre-orogenic fluid migration: Solid Earth, v. 10, p. 1355–1383, doi:10.5194/se-10-1355-2019.

1240 Muchez, P., Slobodnik, M., Viaene, W.A., and Keppens, E., 1995, Geochemical constraints on the
1241 origin and migration of palaeofluids at the northern margin of the Variscan foreland, southern
1242 Belgium: Sedimentary Geology, v. 96, p. 191–200, doi:10.1016/0037-0738(94)00118-E.
1243 O'Neil, J.R., Clayton, R.N., and Mayeda, T.K., 1969, Oxygen isotope fractionation in divalent
1244 metal carbonates: The Journal of Chemical Physics, v. 51, p. 5547–5558,
1245 doi:10.1063/1.1671982.
1246 Palhano, L.C., Nogueira, F.C.C., Marques, F.O., Vasconcelos, D.L., Bezerra, F.H., Souza, J.A.B.,
1247 Nicchio, M.A., Perez, Y.A.R., and Balsamo, F., 2023, Influence of hydrothermal silicification
1248 on the physical properties of a basin-boundary fault affecting arkosic porous sandstones, Rio
1249 do Peixe Basin, Brazil: Marine and Petroleum Geology, v. 148, p. 106062,
1250 doi:10.1016/j.marpetgeo.2022.106062.
1251 Di Paolo, L., Aldega, L., Corrado, S., and Mastalerz, M., 2012, Maximum burial and unroofing of
1252 Mt. Judica recess area in Sicily: implication for the Apenninic-Maghrebian wedge dynamics:
1253 Tectonophysics, v. 530–531, p. 193–207, doi:10.1016/j.tecto.2011.12.020.
1254 Papoulis, D., and Tsolis-Katagas, P., 2008, Formation of alteration zones and kaolin genesis,
1255 Limnos Island, northeast Aegean Sea, Greece: Clay Minerals, v. 43, p. 631–646,
1256 doi:10.1180/claymin.2008.043.4.08.
1257 Pavlides, S., Mountrakis, D., Kilias, A., and Tranos, M., 1990, The role of strike-slip movements
1258 in the extensional area of Northern Aegean (Greece). A case of transtensional tectonics:
1259 Annales Tectonicae, v. 4, p. 196–211.
1260 Pavlides, S., and Tranos, M.D., 1991, Structural characteristics of two strong earthquakes in the
1261 North Aegean: Ierissos (1932) and Agios Efstratios (1968): Journal of Structural Geology, v.
1262 13, p. 205–214, doi:https://doi.org/10.1016/0191-8141(91)90067-S.

1263 Pavlides, S., Tsapanos, T., Zouros, N., Sboras, S., Koravos, G., and Chatzipetros, A., 2009, Using
1264 active fault data for assessing seismic hazard: a case study from NE Aegean Sea, Greece:
1265 Earthquake Geotechnical Engineering Satellite Conference XVIIth International Conference
1266 on Soil Mechanics & Geotechnical Engineering, 2-3 October 2009, Egypt, p. 2–3.
1267 Pe-Piper, G., Piper, D.J.W., Koukouvelas, I., Dolansky, L.M., and Kokkalas, S., 2009,
1268 Postorogenic shoshonitic rocks and their origin by melting underplated basalts: The Miocene
1269 of Limnos, Greece: Bulletin of the Geological Society of America, v. 121, p. 39–54,
1270 doi:10.1130/B26317.1.
1271 Peacock, D.C.P., Dimmen, V., Rotevatn, A., and Sanderson, D.J., 2017, A broader classification
1272 of damage zones: Journal of Structural Geology, v. 102, p. 179–192,
1273 doi:10.1016/j.jsg.2017.08.004.
1274 Perri, F., Caracciolo, L., Cavalcante, F., Corrado, S., Critelli, S., Muto, F., and Dominici, R., 2016,
1275 Sedimentary and thermal evolution of the Eocene-Oligocene mudrocks from the
1276 southwestern Thrace Basin (NE Greece): Basin Research, v. 28, p. 319–339,
1277 doi:10.1111/bre.12112.
1278 Person, M., Hofstra, A., Sweetkind, D., Stone, W., Cohen, D., Gable, C.W., and Banerjee, A.,
1279 2012, Analytical and numerical models of hydrothermal fluid flow at fault intersections:
1280 Geofluids, v. 12, p. 312–326, doi:10.1111/gfl.12002.
1281 Philit, S., Soliva, R., Labaume, P., Gout, C., and Wibberley, C., 2015, Relations between shallow
1282 cataclastic faulting and cementation in porous sandstones: First insight from a groundwater
1283 environmental context: Journal of Structural Geology, v. 81, p. 89–105,
1284 doi:10.1016/j.jsg.2015.10.001.
1285 Pirajno, F., 2009, Hydrothermal processes and mineral systems: Springer Dordrecht, 1250 p.,

doi:10.1007/978-1-4020-8613-7.

Pizzati, M., Balsamo, F., Storti, F., and Iacumin, P., 2019, Physical and chemical strain-hardening during faulting in poorly lithified sandstone: The role of kinematic stress field and selective cementation: Bulletin of the Geological Society of America, v. 132, p. 1183–1200, doi:10.1130/B35296.1.

Salomon, E., Rotevatn, A., Kristensen, T.B., Grundvåg, S., and Henstra, G.A., 2020, Fault-controlled fluid circulation and diagenesis along basin-bounding fault systems in rifts – insights from the East Greenland rift system: Solid Earth, v. 11, p. 1987–2013, doi:https://doi.org/10.5194/se-11-1987-2020.

Schito, A., Andreucci, B., Aldega, L., Corrado, S., Di Paolo, L., Zattin, M., Szaniawski, R., Jankowski, L., and Mazzoli, S., 2018, Burial and exhumation of the western border of the Ukrainian Shield (Podolia): a multi-disciplinary approach: Basin Research, v. 30, p. 532–549, doi:10.1111/bre.12235.

Sharp, Z.D., 1990, A laser-based microanalytical method for the in situ determination of oxygen isotope ratios of silicates and oxides: Geochimica et Cosmochimica Acta, v. 54, p. 1353–1357, doi:10.1016/0016-7037(90)90160-M.

Sharp, Z.D., Atudorei, V., and Durakiewicz, T., 2001, A rapid method for determination of hydrogen and oxygen isotope ratios from water and hydrous minerals: Chemical Geology, v. 178, p. 197–210, doi:10.1016/S0009-2541(01)00262-5.

Sibson, R.H., 1981, Fluid flow accompanying faulting: field evidence and models: Earthquake prediction: an international review, v. 4, p. 593–603, doi:10.1029/me004p0593.

Sibson, R.H., 2000, Fluid involvement in normal faulting: Journal of Geodynamics, v. 29, p. 469–499, doi:https://doi.org/10.1016/S0264-3707(99)00042-3.

1309 Siyako, M., and Huvaz, O., 2007, Eocene stratigraphic evolution of the Thrace Basin, Turkey:
1310 Sedimentary Geology, v. 198, p. 75–91, doi:10.1016/j.sedgeo.2006.11.008.
1311 Smeraglia, L. et al., 2018, Crustal-scale fluid circulation and co-seismic shallow comb-veining
1312 along the longest normal fault of the central Apennines, Italy: Earth and Planetary Science
1313 Letters, v. 498, p. 152–168, doi:10.1016/j.epsl.2018.06.013.
1314 Smeraglia, L., Bettucci, A., Billi, A., Carminati, E., Cavallo, A., Di Toro, G., Natali, M., Passeri,
1315 D., Rossi, M., and Spagnuolo, E., 2017, Microstructural evidence for seismic and aseismic
1316 slips along clay-bearing, carbonate faults: Journal of Geophysical Research: Solid Earth, v.
1317 122, p. 3895–3915, doi:10.1002/2017JB014042.
1318 Suh, C.E., and Dada, S.S., 1997, Fault rocks and differential reactivity of minerals in the Kanawa
1319 Violaine uraniferous vein, NE Nigeria: Journal of Structural Geology, v. 19, p. 1037–1044,
1320 doi:10.1016/S0191-8141(97)00010-2.
1321 Sutherland, R. et al., 2012, Drilling reveals fluid control on architecture and rupture of the Alpine
1322 fault, New Zealand: Geology, v. 40, p. 1143–1146, doi:10.1130/G33614.1.
1323 Sutherland, R. et al., 2017, Extreme hydrothermal conditions at an active plate-bounding fault:
1324 Nature, v. 546, p. 137–140, doi:10.1038/nature22355.
1325 Suzuoki, T., and Epstein, S., 1976, Hydrogen isotope fractionation between OH-bearing minerals
1326 and water: Geochimica et Cosmochimica Acta, v. 40, p. 1229–1240, doi:10.1016/0016-
1327 7037(76)90158-7.
1328 Taylor, H. P. Jr (1979) Oxygen and hydrogen isotope relationships in hydrothermal mineral
1329 deposits *in* Barnes, H.L., eds., Geochemistry of Hydrothermal Ore Deposits, John Wiley,
1330 London, p. 236–277.
1331 Taymaz, T., Jackson, J., and McKenzie, D., 1991, Active tectonics of the north and central Aegean

Sea: Geophysical Journal International, v. 106, p. 433–490, doi:10.1111/j.1365-246X.1991.tb03906.x.

Taymaz, T., Yilmaz, Y., and Dilek, Y., 2007, The geodynamics of the Aegean and Anatolia: Introduction: Geological Society Special Publication, v. 291, p. 1–16, doi:10.1144/SP291.1.

Toby, B.H., and Von Dreele, R.B., 2013, GSAS-II: The genesis of a modern open-source all purpose crystallography software package: Journal of Applied Crystallography, v. 46, p. 544–549, doi:10.1107/S0021889813003531.

Torabi, A., and Berg, S.S., 2011, Scaling of fault attributes: A review: Marine and Petroleum Geology, v. 28, p. 1444–1460, doi:10.1016/j.marpetgeo.2011.04.003.

Tranos, M.D., 2009, Faulting of Lemnos Island; a mirror of faulting of the North Aegean Trough (Northern Greece): Tectonophysics, v. 467, p. 72–88, doi:10.1016/j.tecto.2008.12.018.

Travé, A., Labaume, P., and Vergés, J., 2007, Fluid Systems in Foreland Fold-and-Thrust Belts: An Overview from the Southern Pyrenees, *in* Thrust Belts and Foreland Basins, p. 91–113, doi:10.1007/978-3-540-69426-7.

Vennemann, T.W., and O'Neil, J.R., 1996, Hydrogen isotope exchange reactions between hydrous minerals and molecular hydrogen: I. A new approach for the determination of hydrogen isotope fractionation at moderate temperatures: Geochimica et Cosmochimica Acta, v. 60, p. 2437–2451, doi:10.1016/0016-7037(96)00103-2.

Verlaguet, A., Bonnemains, D., Mével, C., Escartín, J., Andreani, M., Bourdelle, F., Boiron, M.C., and Chavagnac, V., 2021, Fluid Circulation Along an Oceanic Detachment Fault: Insights From Fluid Inclusions in Silicified Brecciated Fault Rocks (Mid-Atlantic Ridge at 13°20′N): v. 22, 1–32 p., doi:10.1029/2020GC009235.

Vignaroli, G., Viola, G., Diamanti, R., Zuccari, C., Garofalo, P.S., Bonini, S., and Selli, L., 2020,

Multistage strain localisation and fluid-assisted cataclasis in carbonate rocks during the seismic cycle: Insights from the Belluno Thrust (eastern Southern Alps, Italy): Journal of Structural Geology, v. 141, p. 104216, doi:10.1016/j.jsg.2020.104216.

Voudouris, P., and Alfieris, D., 2005, New porphyry - Cu ± Mo occurrences in the north-eastern Aegean, Greece: Ore mineralogy and epithermal relationships, *in* Mineral Deposit Research: Meeting the Global Challenge, doi:10.1007/3-540-27946-6.

Williams, R.T., and Fagereng, Å., 2022, The Role of Quartz Cementation in the Seismic Cycle: A Critical Review: Reviews of Geophysics, v. 60, doi:10.1029/2021RG000768.

Williams, R.T., Goodwin, L.B., and Mozley, P.S., 2017, Diagenetic controls on the evolution of fault-zone architecture and permeability structure: Implications for episodicity of fault-zone fluid transport in extensional basins: Bulletin of the Geological Society of America, v. 129, p. 464–478, doi:10.1130/B31443.1.

Worden, R.H., and Morad, S., 2009, Quartz Cementation in Oil Field Sandstones: A Review of the Key Controversies, *in* Worden, R.H., and Morad, S., eds., Quartz Cementation in Sandstones, Special Publication of the Internationl Association of Sedimentologists 29, p. 1–20, doi:10.1002/9781444304237.ch1.

Yeh, H.-W., 1980, D / H Ratios and late-stage dehydration of shales during burial Sample preparation: Geochimica et Cosmochimica Acta, v. 44, p. 341–352, doi:10.1016/0016-7037(80)90142-8.

You, D., Han, J., Hu, W., Qian, Y., Chen, Q., Xi, B., and Ma, H., 2018, Characteristics and formation mechanisms of silicified carbonate reservoirs in well SN4 of the Tarim Basin: Energy Exploration and Exploitation, v. 36, p. 820–849, doi:10.1177/0144598718757515.

FIGURE CAPTIONS

Figure 1. (A) Simplified geological map of Lemnos Island redrawn after Innocenti et al. (1994, 2009). The black square indicates the study area and the black arrows the Kornos-Aghios Ioannis Fault (KAIF). NAF: Northern Anatolian Fault. Focal mechanisms are from Pavlides et al. (1990) and Koukouvelas and Aydin (2002). A sampling site for host rock collected far away from the KAIF is indicated by the red star. (B) Stratigraphic column of the Cenozoic units exposed on Lemnos Island redrawn after Innocenti et al. (1994). (C) Satellite image of the study area overlain by a simplified geological map redrawn and modified after Innocenti et al. (1994, 2009). The image shows the overall 2D geometry of the KAIF and the location of the sampling sites (see figure legend for details). Cumulative stereonets showing the attitude and kinematics of principal slip surfaces in sectors A, B and C are from Berio et al. (2023). Structural data are reported according to the right-hand rule (strike/dip) and are shown in lower hemisphere stereographic projections (Schmidt net). Red squares indicate the orientation of the slickenlines on principal slip surfaces and the normal kinematics. Red great circles represent the mean fault plane for each sector and the white squares the mean pitch value.

Figure 2. Panoramic views of the KAIF fault and silicified domains. (A) Panoramic view of sector A (tip region) showing the principal slip surface, and the footwall damage zone massively affected by silicification. (B) Cross-sectional view of the fault in sector B showing the normal drag of bedding planes, the silicified fault core and the silicification of the turbidite sequence in the hanging wall and in the footwall damage zone. Note that in the footwall, silicification preferentially affects fine- to medium-grained sandstones compared to mudstone layers forming irregular geometries. The red and white dashed lines bound the silicified domains. See **figure 1** for the location of the panoramic views. MSS-Massively Silicified Sandstone; MSFC-Massively Silicified Fault Core.

Figure 3. Hand samples (fresh section cuts) and outcrop images showing the host rock and five main types of hydrothermally altered fault-related rocks mapped and sampled along the KAIF. Locations are shown in **figures 1-2**. (A) Outcrop image showing the host rock not affected by hydrothermal alteration far away from fault zones and volcanic intrusions. (B) Outcrop image showing massively silicified turbidite sandstones in fault damage zones. (C) Fresh section cut of a massively silicified ultracataclasite with silica and quartz clasts in a silicified matrix. The white arrow indicates that the principal normal slip surface is located at the upper boundary of the image.

(D) Outcrop image of medium-grained sandstone strata affected by advanced argillic alteration. The sandstones are intensively micro-fractured, locally forming breccia pockets cemented by silica and iron oxides. Breccia pockets are delimited by blue dashed lines. (E) Outcrop image of quartz-cemented crackle breccias developed in the damage zones at the expense of the massively silicified sandstones. Note the vuggy porosity marked by red haloes. (F) Fresh section cut of a partially silicified fault core that contains centimeter-scale clasts derived from massively silicified fault core rocks. The dashed red lines delimit the regions that are silicified. Meaning of the abbreviations: MSS-Massively Silicified Sandstone; MSFC-Massively Silicified Fault Core; QZCB-Quartz-cemented Crackle Breccia.

Figure 4. Outcrop images showing two types of hydrothermally altered fault-related rocks. Locations are shown in **figures 1-3.** (A) Example of a partially silicified to non-silicified fault core made up of a poorly cohesive fault gouge bounded by a 10 cm-thick massively silicified fault core made up of cataclasites. (B) Vein stockwork in the hanging wall damage zone of sector A. Veins are filled by calcite and barite. Coin for scale. (C) Decimeter-scale vein in the hanging wall damage zone of sector C filled by quartz, calcite, and dolomite.

Figure 5. Panoramic views of the silicified segments of the KAIF in different sectors. (A) Panoramic view in sector B showing the silicified principal slip surface and the extension of fault-related lithotypes. (B) Panoramic view in the tip-region of the KAIF (sector A) showing multiple fault strands and the extension of fault-related lithotypes. Blue dashed lines indicate the boundary between host rocks and massively silicified sandstones. Red dashed lines indicate the boundary between quartz-cemented crackle breccias and massively silicified sandstones. MSS-Massively Silicified Sandstone; MSFC-Massively Silicified Fault Core; QZCB-Quartz-cemented Crackle Breccia; AAS-Argillic-Altered Sandstone; HR-Host Rock; HW-Hanging Wall; FW-Footwall.

Figure 6. Satellite images showing the distribution and thickness of fault-related lithotypes along the silicified domain of the KAIF. See **figure 1c** for the location of the images. (A) Sector A. (B) Sector B.

Figure 7. Thin section scans and microphotographs showing examples of host rocks and massively silicified sandstones. (A) Thin section scan of a sandstone host rock of the Fissini-Sardes unit impregnated with blue epoxy resin. Note the porosity (P). (B) Thin section scan of a massively silicified turbidite sandstone impregnated with blue epoxy resin. (C) Microphotograph in cross-polarized light of a silicified sandstone cemented by microcrystalline silica (μqz) and quartz (qz).

Note pyrite crystals (py). (D) Microphotograph in cross-polarized light of quartz cements (red arrows) occluding porosity.

Figure 8. Microphotographs of examples of massively silicified fault rocks. (A) Backscattered electron (BSE) image of the silicified matrix of a silicified cataclasite showing quartz (qz), pyrite (py) and relict feldspars (fld). (B) Microphotograph in cross-polarized light of a massively silicified ultracataclasite showing its silicified matrix made up of microcrystalline silica (μqz) with a relict plagioclase crystal characterized by a corroded outer margin. (C) Microphotograph in cross-polarized light of a dilatant silicified cataclasite on the principal slip surface showing the crystallization sequence microcrystalline silica → chalcedony → euhedral quartz. The porosity is only partially filled by iron oxides. Blue and red arrows indicate chalcedony and iron oxides respectively cementing microveins that post-date silicification. (D) Microphotograph in cross-polarized light of a silicified cataclasite showing rounded silicified clasts with embayments in a silicified matrix. (E) Micrograph in plane polarized light of a silicified cataclasite containing a clast of a silicified cataclasite. (F) Microphotograph in plane polarized light of the principal slip surface coated by microcrystalline silica. Sandstone clasts are sharply truncated by the slip surface. μqz-microcrystalline silica; ch-chalcedony; qz-quartz; Fe-ox-iron oxide; P-porosity.

Figure 9. Microphotographs and thin section scans of massively silicified fault rocks and quartz-cemented crackle breccias. (A) Thin section scan of a quartz-cemented crackle breccia developed in the damage zones at the expenses of the massively silicified sandstones. The breccia is cemented by microcrystalline silica and quartz. (B) Microphotograph in cross-polarized light of quartz cement with feathery texture in a crackle breccia. See (A) for micrograph location. (C) Thin section scan of a silicified ultracataclasite affected by brecciation on the principal slip surface (red arrow). The breccia is cemented by microcrystalline silica and quartz and the vugs are partially filled by iron oxides. Note the deformation gradient towards the principal slip surface. (D) Thin section scan of a silicified cataclasite on principal slip surface (red arrow) grading into volcanic host rock towards the right. Volcanic host rock is deformed by several microveins cemented by quartz and microcrystalline silica. μqz-microcrystalline silica; ch-chalcedony; qz-quartz; Fe-ox-iron oxide.

Figure 10. Microphotographs and thin section scans of partially silicified fault core rocks (PSFC) locally showing iron oxides/hydroxides mineralization and K-bearing micas. (A) Backscattered electron (BSE) image of two domains of PSFC: (i) domain mineralized by K-bearing mica and quartz, (ii) domain silicified. See (B) for micrograph location. (B) Thin section scan showing three

distinct mineralized domains in PSFC. (C) Microphotograph in plane polarized light of K-bearing mica and quartz. See (B) for micrograph location. (D) Backscattered electron (BSE) image of two domains of PSFC: (i) the domain mineralized by iron oxides/hydroxides and quartz, (ii) the domain mineralized by K-bearing mica and quartz. See (B) for micrograph location.

Figure 11. Microphotographs and thin section scans showing petrography of veins in vein stockworks (VS) within fault damage zones. (A) Thin section scan of a quartz filled vein sampled in the footwall damage zone. Red arrows indicate several micro-veins cemented by iron-oxides that cross-cut the quartz-filled vein. (B) Thin section scan of a vein in the hanging wall damage zone filled by blocky calcite (BC), acicular/bladed calcite (AC) and barite. (C) CL image of blocky (BC) and acicular (AC) calcite crystals in a vein in the hanging wall damage zone. (D) CL image of blocky calcite (BC), dolomite (dol) and microcrystalline silica (μqz) in a vein in the hanging wall damage zone.

Figure 12. Spatial variation in quartz, K-feldspar, plagioclase, chlorite, and muscovite content (wt. %) from whole-rock XRD analysis along two fault perpendicular transects in the footwall damage zone of the KAIF fault. The principal slip surface is located at the origin of the x axis. The dashed red lines indicate the host rock-damage zone boundaries for sector B and A from Berio et al. (2023). (A) Fault perpendicular transect in the footwall wall damage zone of sector B. (B) Fault perpendicular transect in the footwall tip damage zone of sector A. See **figure 2** for transect location.

Figure 13. (A-B) Microphotographs showing the primary fluid inclusion assemblages (FIA) containing two-phase liquid-vapor inclusions in calcite cements. (C-D) Microthermometric characteristics of the measured inclusions in calcite (red symbols) and quartz (black symbols) subdivided by fluid inclusion assemblage (FIA) and by sample: (C) homogenization temperatures (Th); (D) melting temperatures of clathrates ($Tm_{ice/cla}$). The blue lines indicate the mean value of each fluid inclusion assemblage. The number of inclusions in each fluid inclusion assemblage is indicated.

Figure 14. Stable isotope data of calcite and silica cements and isotopic signature recalculated for the fluids. (A) $\delta^{13}C$ and $\delta^{18}O$ crossplot of calcite cements. V-PDB stands for Vienna Pee Dee belemnite. (B) Inter-quartile box-whisker plot of $\delta^{18}O$ data of silica cements. SMOW stands for Standard Mean Ocean Water. (C) Inter-quartile box-whisker plot of the calculated $\delta^{18}O$ signatures of the fluid from those of the calcite cements assuming equilibrium precipitation and using mean

fluid temperatures from fluid inclusion microthermometry (O'Neil et al., 1969). (D) Inter-quartile box-whisker plot of the calculated $\delta^{18}O$ signatures of the fluid from those of the silica cements assuming equilibrium precipitation and using mean fluid temperatures from fluid inclusion microthermometry (Clayton et al., 1972).

Figure 15. (A) Inter-quartile box-whisker plots showing the trace element concentration (Mg, Mn, Fe and Sr) in calcite cements. (B-C) Chondrite-normalized REE patterns of carbonate cements (calcite and dolomite) sampled in veins. (D) Comparison of chondrite-normalized patterns of the analyzed carbonate cements with those of volcanic rocks (Myrina Unit) from Pe-Piper et al. (2009).

Figure 16. Evolutionary model of the silicification process across the KAIF. For each schematic cross-section, a schematic map-view sketch showing the areal distribution of hydrothermally altered and silicified rocks is reported. (A) Onset of extensional deformation and development of a fractured damage zone. (B) Formation of the hydrothermally altered and silicified zone. (C) Fluid pressure buildup and hydrofracturing with development of crackle breccia textures and vein stockworks in the pre-seismic phase followed by coseismic rupturing. (D) More recent fault activity still characterized by hydrothermal fluid circulation, but lacking extensive silica cementation. Development of partially silicified to non-silicified fault cores and veins filled by iron oxides. Stages (B) and (C) are cyclic implying multiple hydrothermal pulses/cementation events. Meaning of abbreviations: MSS-Massively Silicified Sandstone; MSFC-Massively Silicified Fault Core; QZCB-Quartz-cemented Crackle Breccia; AAS-Argillic-Altered Sandstone; PSFC-Partially Silicified to non-silicified Fault Core; Fe-ox-Iron-Oxides.

[1]Supplemental Material includes the complete geochemical data set and additional information on *in situ* LA-ICP-MS analyses. Please visit https://doi.org/10.1130/XXXX to access the supplemental material, and contact editing@geosociety.org with any questions.

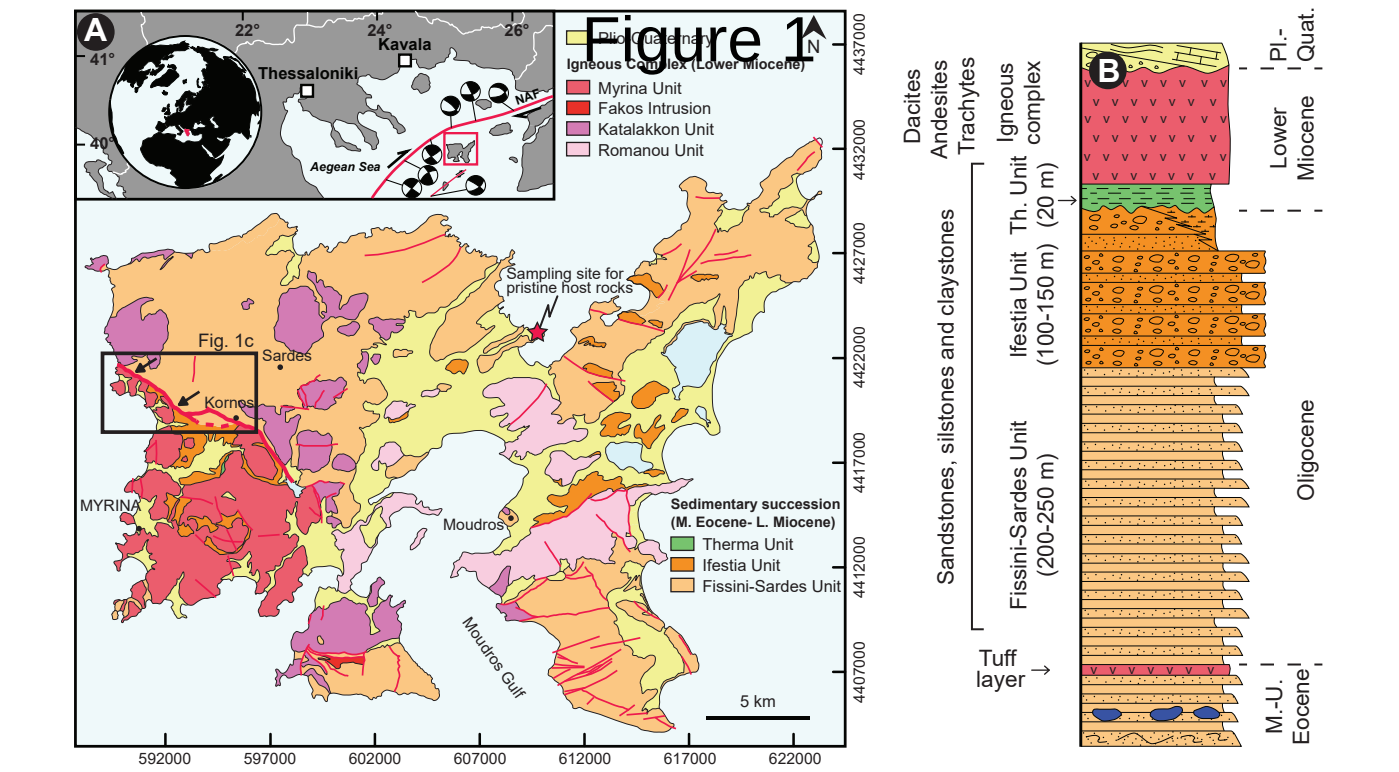

Figure 1

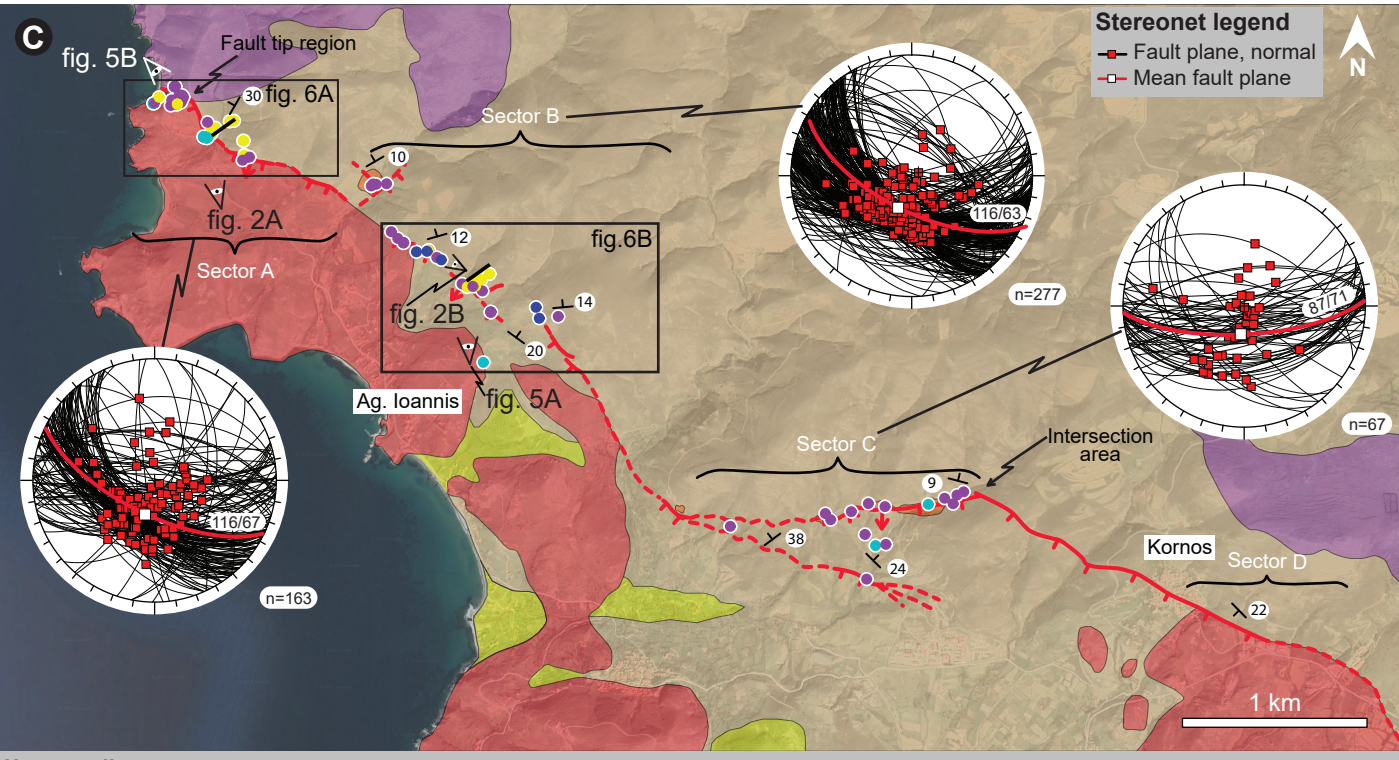

Upper sedimentary sequence:
- Quaternary deposits

Igneous Complex:
- Dacite, andesite (Myrina Unit, L. Miocene)
- Dacite, andesite (Katalakkon Unit, L. Miocene)
- Dacite, andesite and trachyte of unknwown age

U. Eocene-L.Oligocene turbidite deposits:
- Ifestia and Fissini-Sardes Unit

- Normal fault: (a) certain, (b) interpreted
- Bedding
- Mineralogical transect

Samples
- Petrography and microstructural analysis
- Petrography, geochemistry and fluid inclusions (carbonates)
- Petrography, geochemistry and fluid inclusions (silica)
- Petrography and mineralogy (XRD)

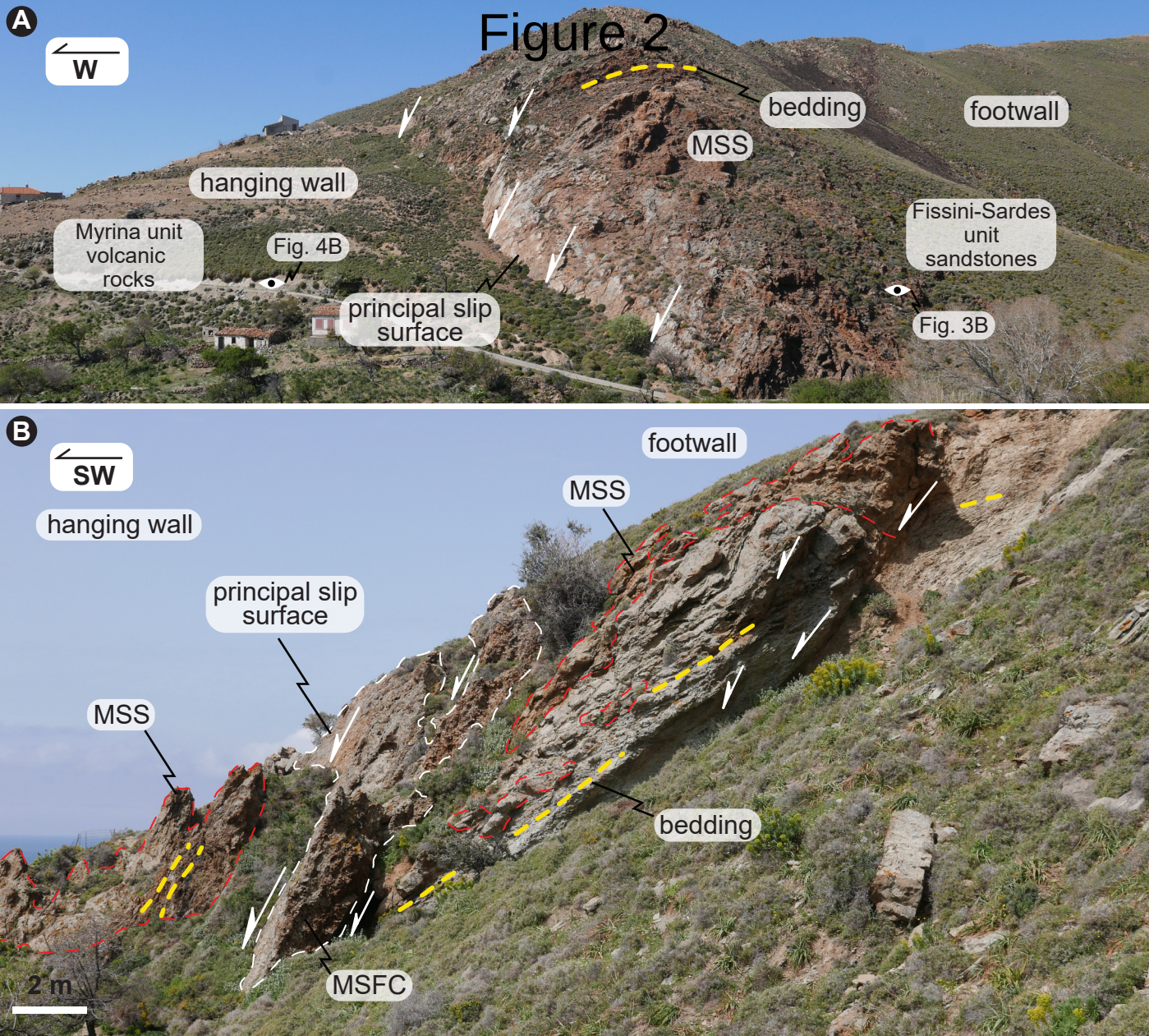
Figure 2
A
W
bedding
footwall
MSS
hanging wall
Myrina unit volcanic rocks
Fig. 4B
principal slip surface
Fissini-Sardes unit sandstones
Fig. 3B
B
SW
footwall
MSS
hanging wall
principal slip surface
MSS
bedding
MSFC
2 m

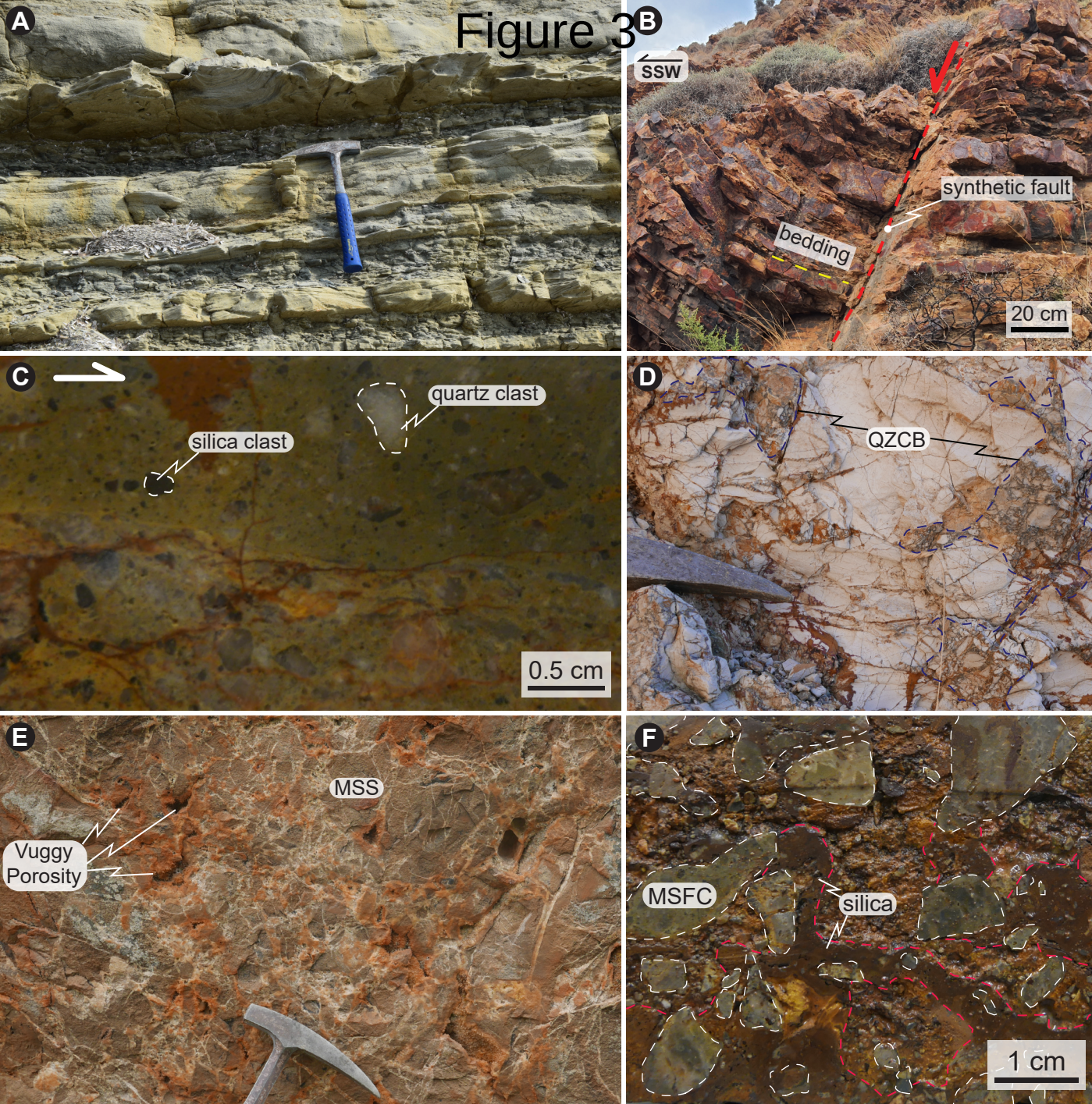
Figure 3
A
B
SSW
synthetic fault
bedding
20 cm
C
quartz clast
silica clast
0.5 cm
D
QZCB
E
MSS
Vuggy
Porosity
F
MSFC
silica
1 cm

Figure 4

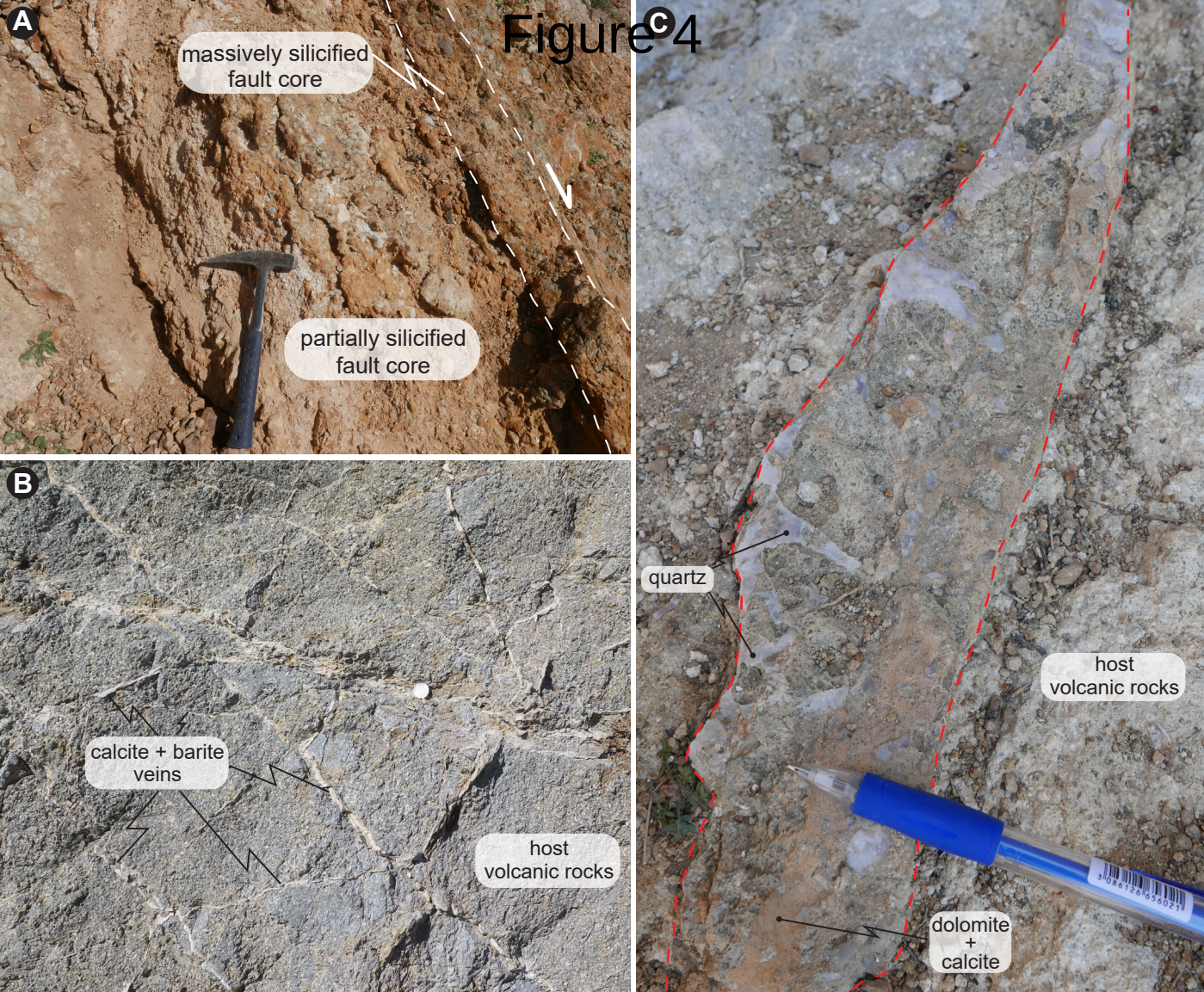
A
massively silicified fault core
partially silicified fault core
B
calcite + barite veins
host volcanic rocks
C
quartz
host volcanic rocks
dolomite + calcite

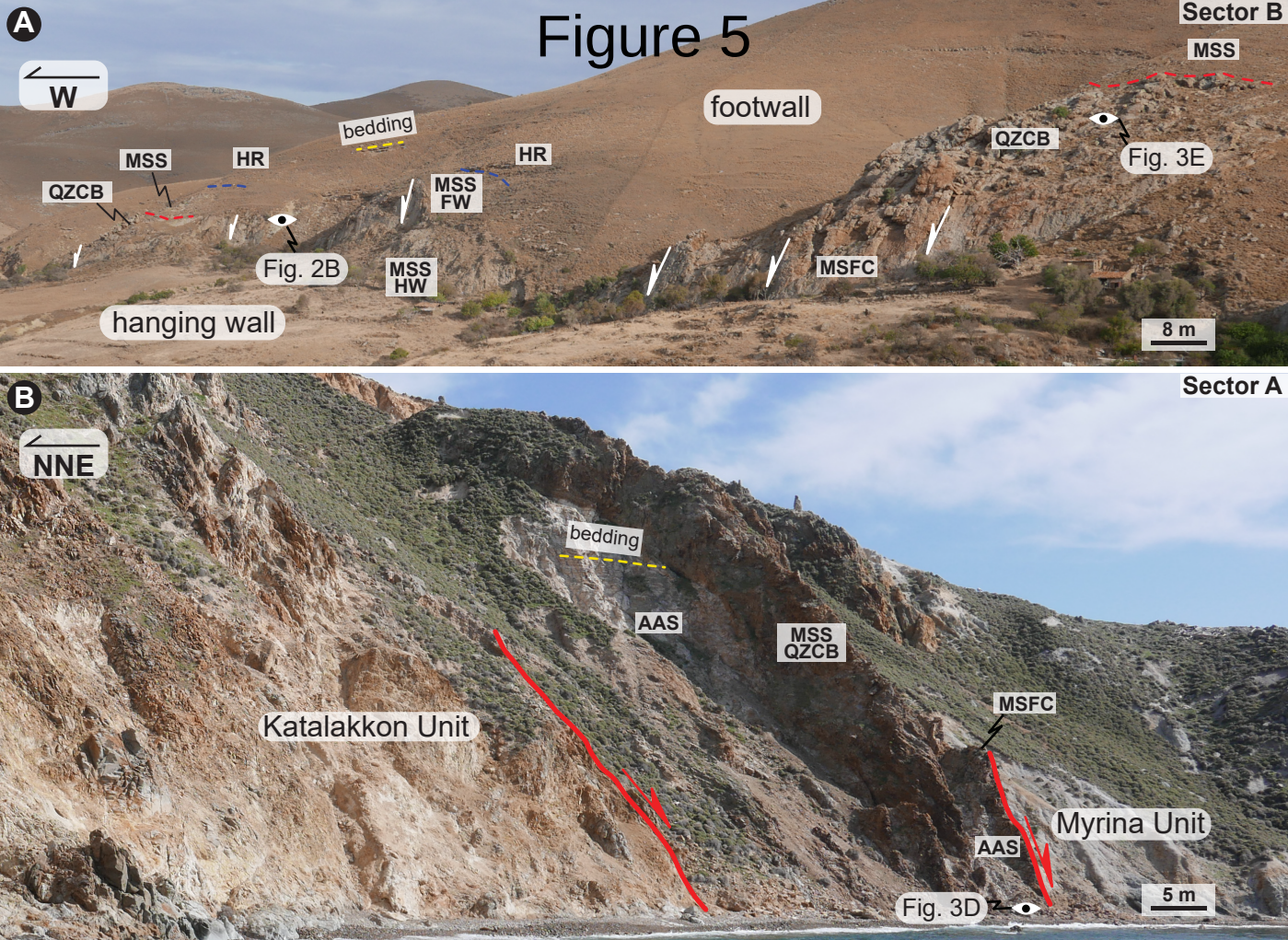
Figure 5
A
W
Sector B
MSS
footwall
bedding
HR
HR
MSS
QZCB
MSS
FW
QZCB
Fig. 3E
Fig. 2B
MSS
HW
MSFC
hanging wall
8 m
B
NNE
Sector A
bedding
AAS
MSS
QZCB
MSFC
Katalakkon Unit
Myrina Unit
AAS
Fig. 3D
5 m

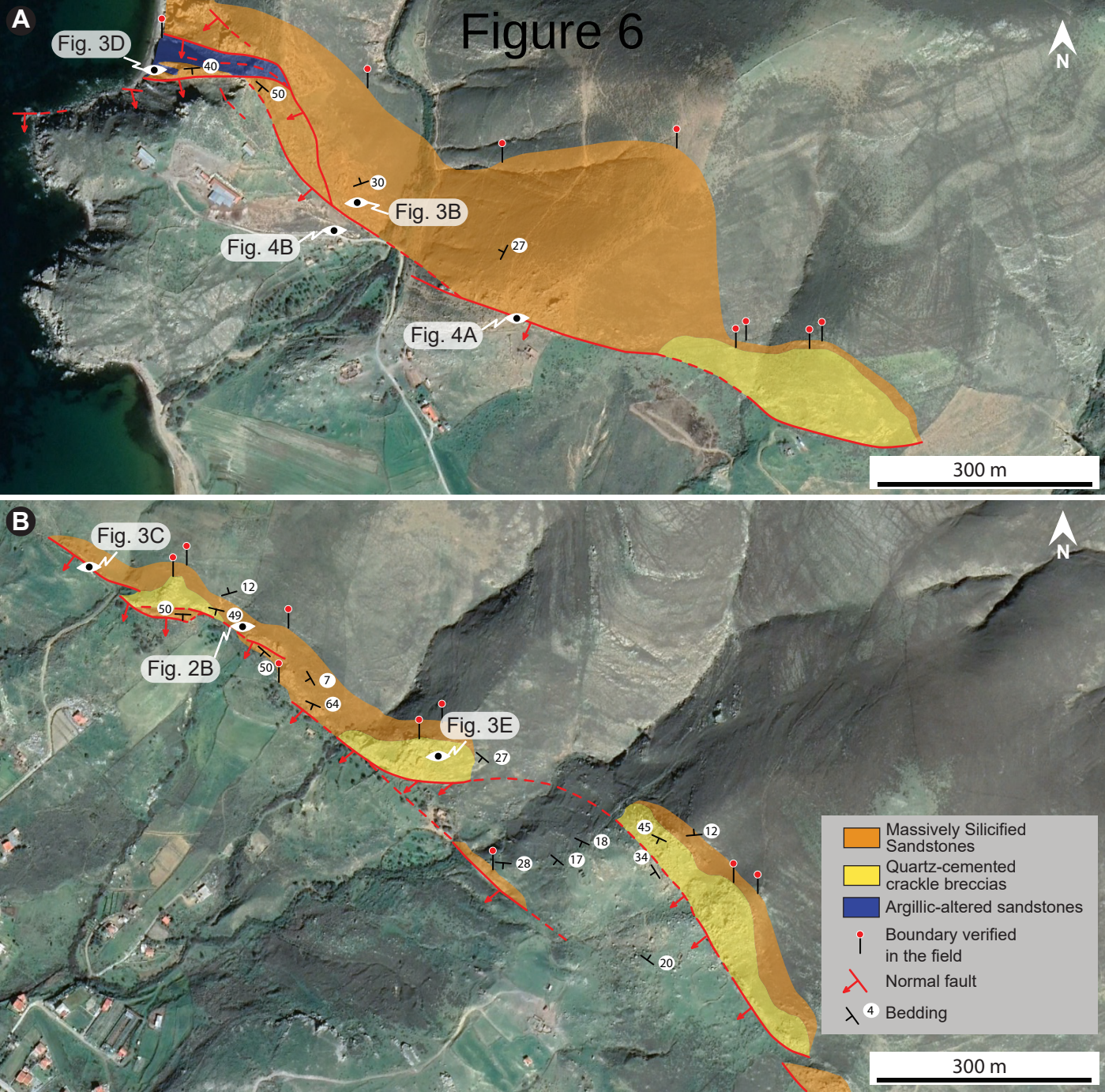
Figure 6
A
Fig. 3D
40
50
30
Fig. 3B
Fig. 4B
27
Fig. 4A
N
300 m
B
Fig. 3C
12
50
49
Fig. 2B
50
7
64
Fig. 3E
27
45
12
18
28
17
34
20
N
Massively Silicified Sandstones
Quartz-cemented crackle breccias
Argillic-altered sandstones
Boundary verified in the field
Normal fault
4
Bedding
300 m

Figure 7

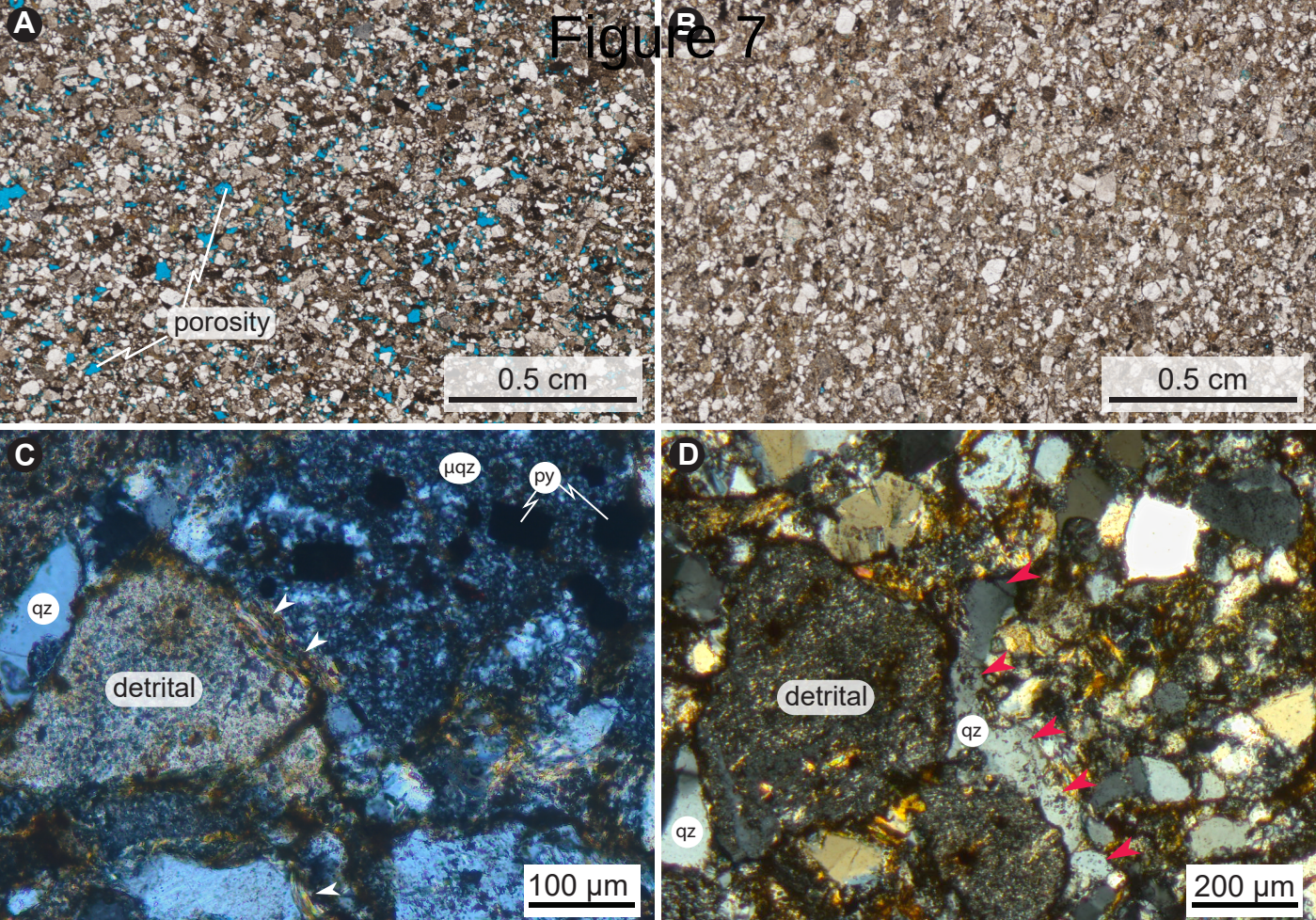
A
porosity
0.5 cm
B
0.5 cm
C
μqz
py
qz
detrital
100 μm
D
detrital
qz
qz
200 μm

Figure 8

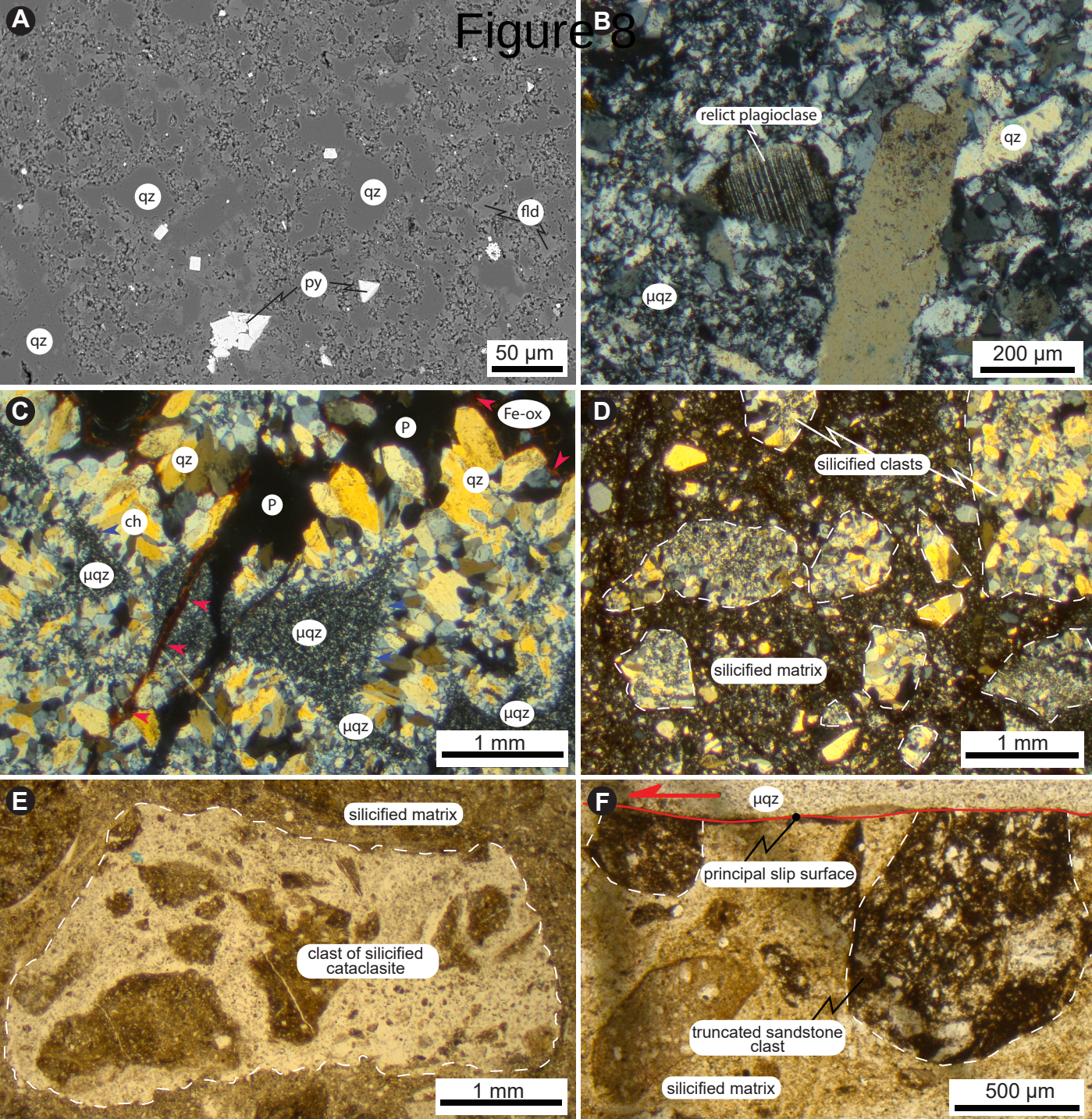
A
qz
qz
fld
py
qz
50 µm
B
relict plagioclase
qz
µqz
200 µm
C
Fe-ox
P
qz
qz
P
ch
µqz
µqz
µqz
µqz
1 mm
D
silicified clasts
silicified matrix
1 mm
E
silicified matrix
clast of silicified cataclasite
1 mm
F
µqz
principal slip surface
truncated sandstone clast
silicified matrix
500 µm

Figure 9

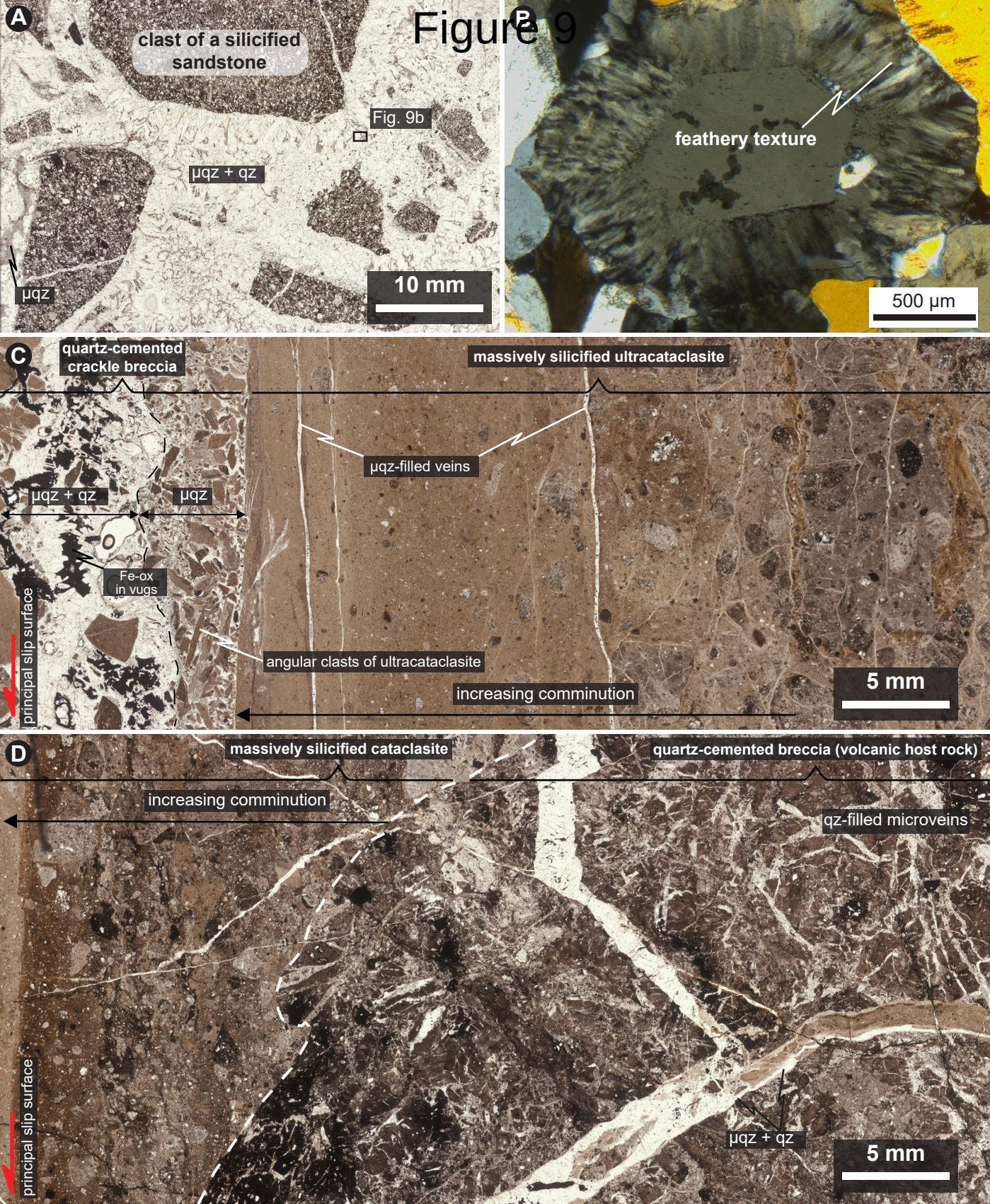
A
clast of a silicified sandstone
Fig. 9b
µqz + qz
µqz
10 mm
B
feathery texture
500 µm
C
quartz-cemented crackle breccia
massively silicified ultracataclasite
µqz-filled veins
µqz + qz
µqz
Fe-ox in vugs
angular clasts of ultracataclasite
increasing comminution
principal slip surface
5 mm
D
massively silicified cataclasite
quartz-cemented breccia (volcanic host rock)
increasing comminution
qz-filled microveins
µqz + qz
principal slip surface
5 mm

Figure 10

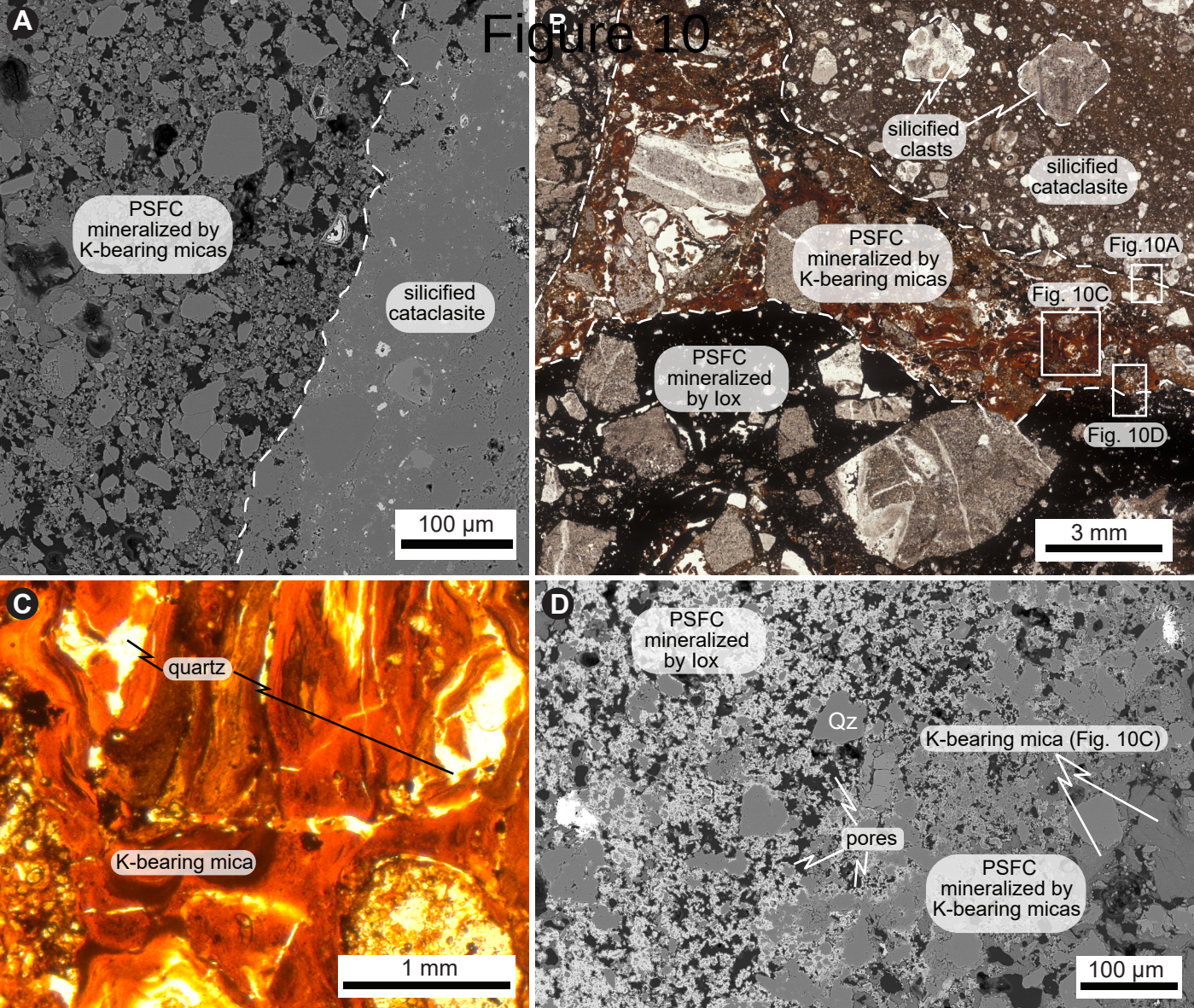
A
PSFC mineralized by K-bearing micas
silicified cataclasite
100 µm
B
silicified clasts
silicified cataclasite
PSFC mineralized by K-bearing micas
Fig.10A
Fig. 10C
PSFC mineralized by lox
Fig. 10D
3 mm
C
quartz
K-bearing mica
1 mm
D
PSFC mineralized by lox
Qz
K-bearing mica (Fig. 10C)
pores
PSFC mineralized by K-bearing micas
100 µm

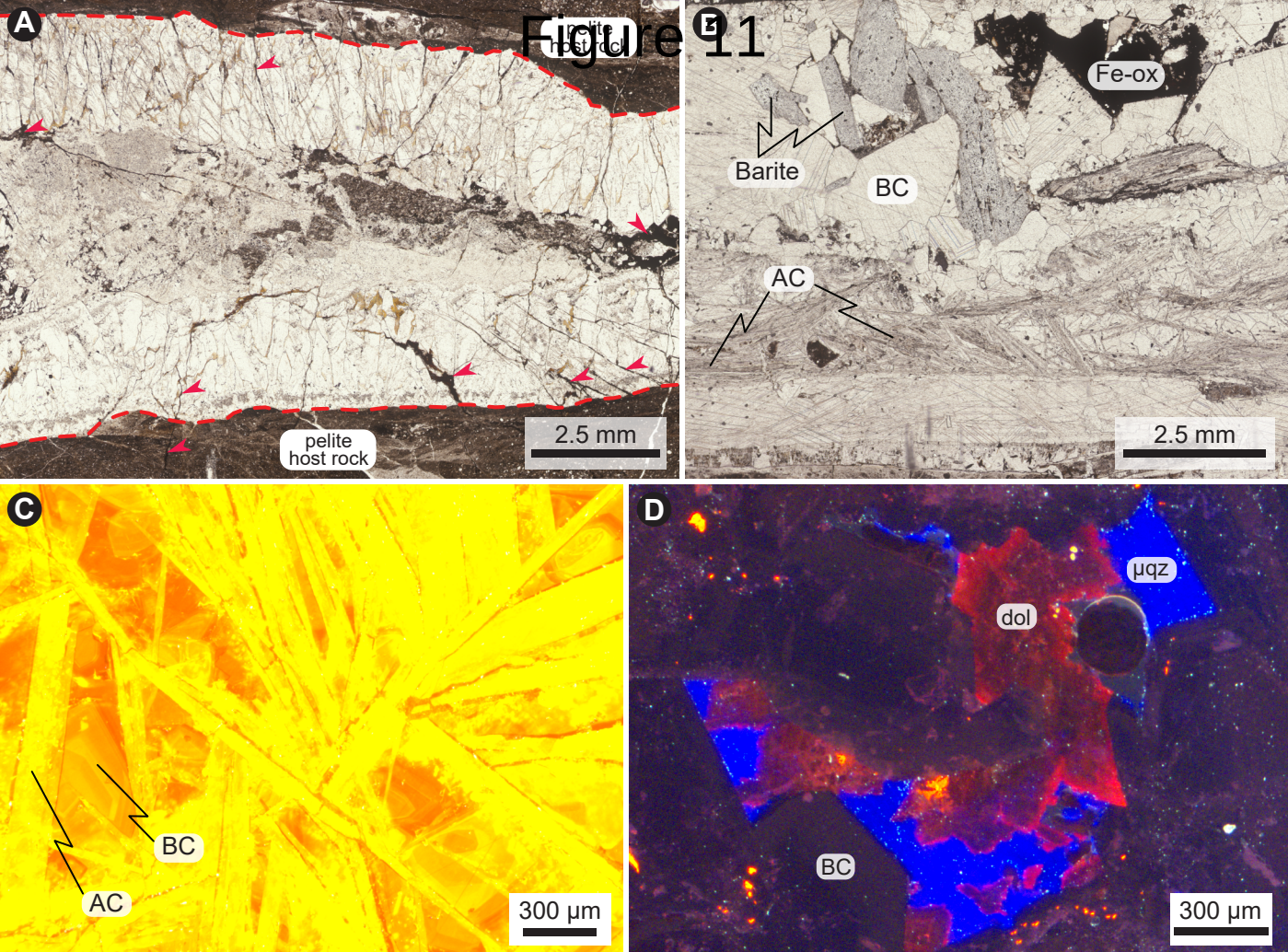
A
pelite host rock
2.5 mm
B
Fe-ox
Barite
BC
AC
2.5 mm
C
BC
AC
300 µm
D
µqz
dol
BC
300 µm

Figure 12

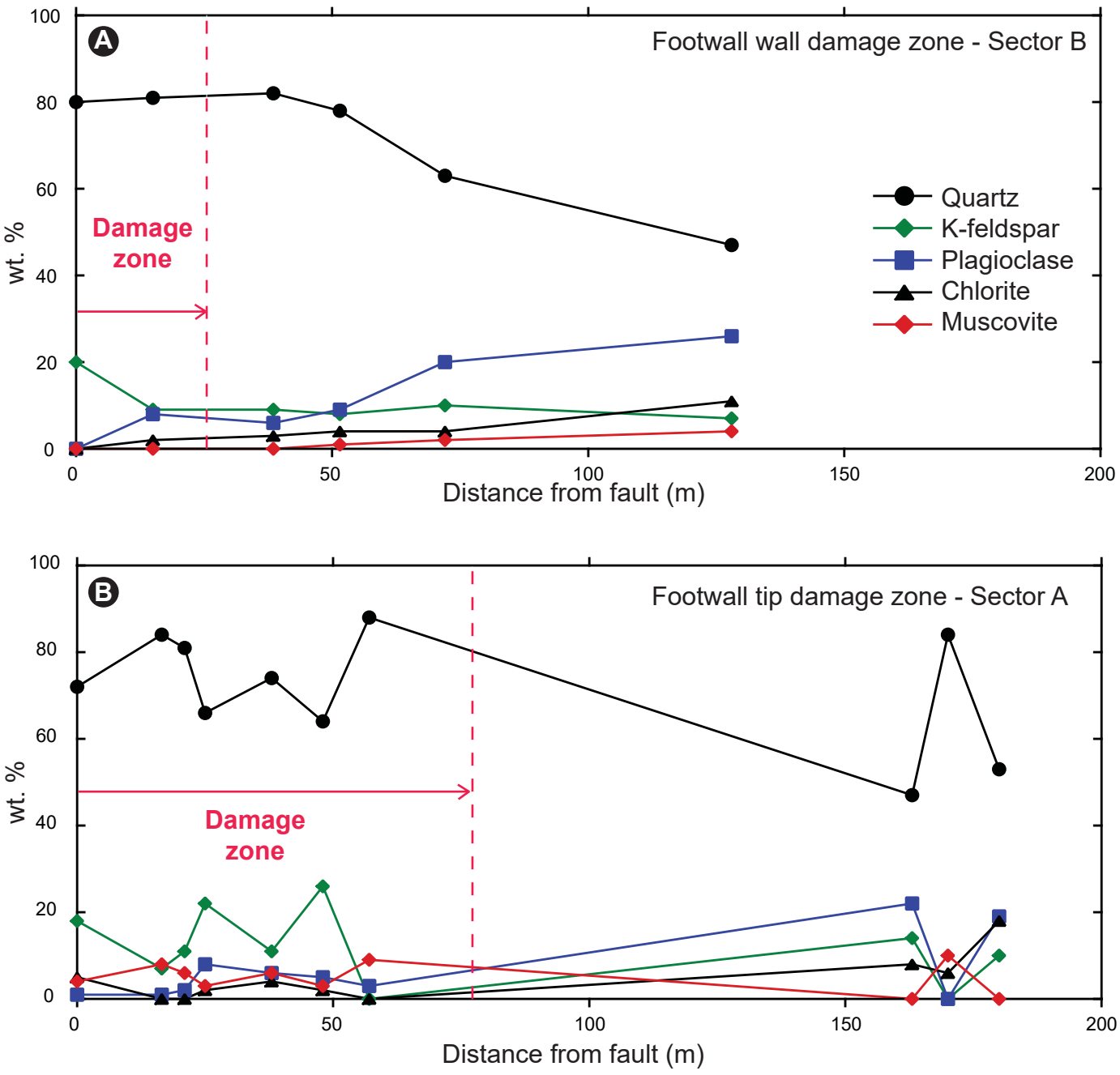
A
Footwall wall damage zone - Sector B
Damage zone
wt. %
Distance from fault (m)
Quartz
K-feldspar
Plagioclase
Chlorite
Muscovite
B
Footwall tip damage zone - Sector A
Damage zone
wt. %
Distance from fault (m)

Figure 13

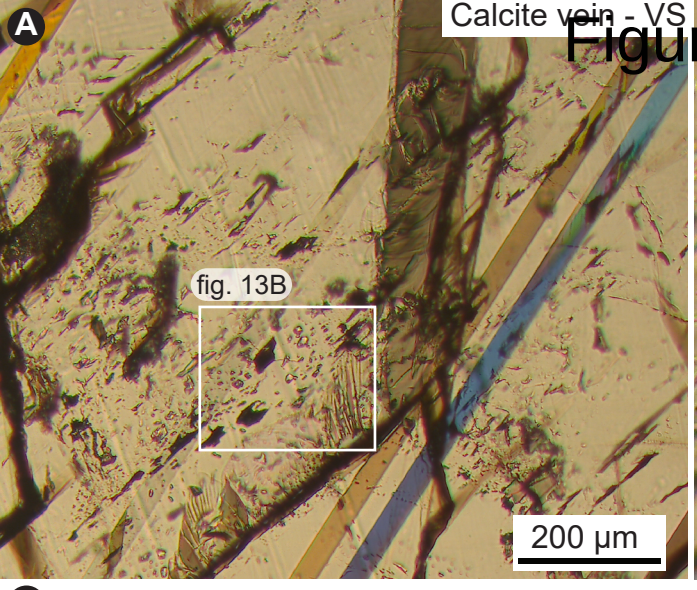
A
Calcite vein - VS
fig. 13B
200 µm

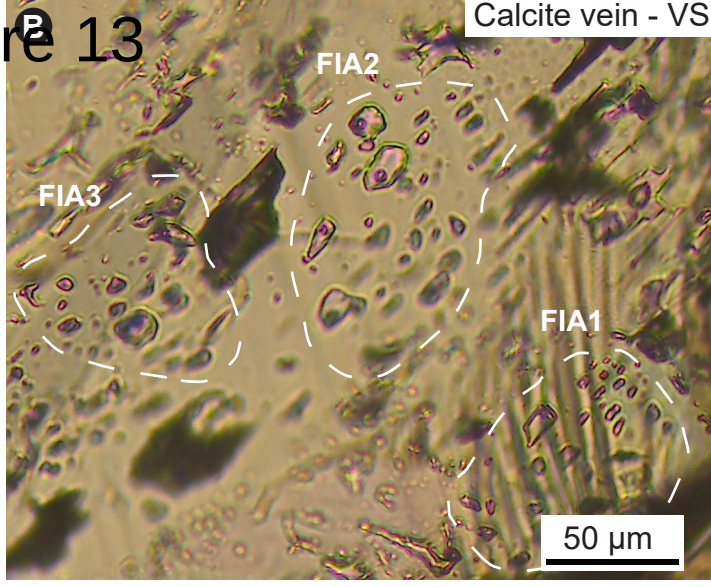
B
Calcite vein - VS
FIA2
FIA3
FIA1
50 µm

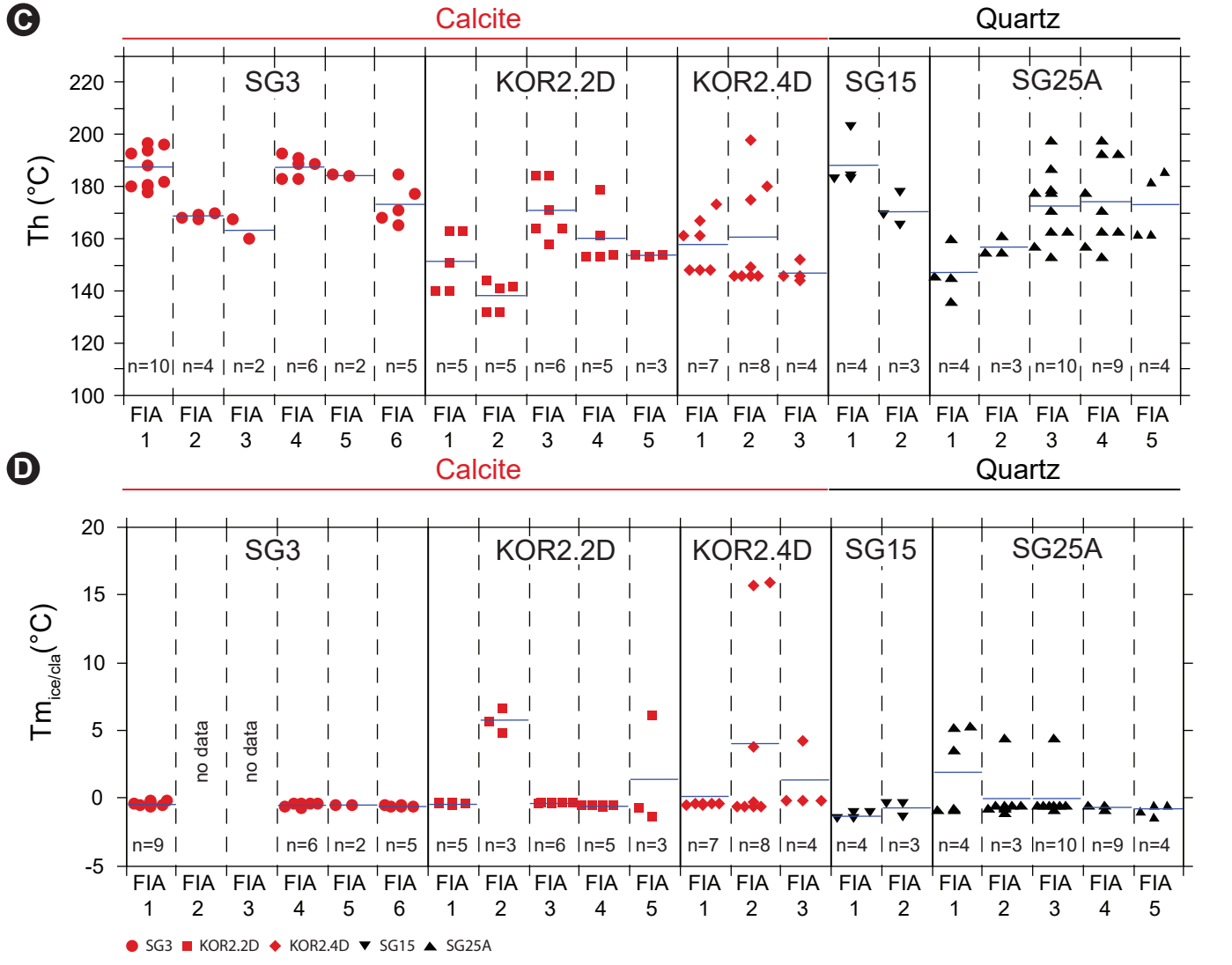
C
Calcite
Quartz
Th (°C)
SG3
KOR2.2D
KOR2.4D
SG15
SG25A
D
Tm ice/cla (°C)
no data
no data
SG3 KOR2.2D KOR2.4D SG15 SG25A

Figure 14

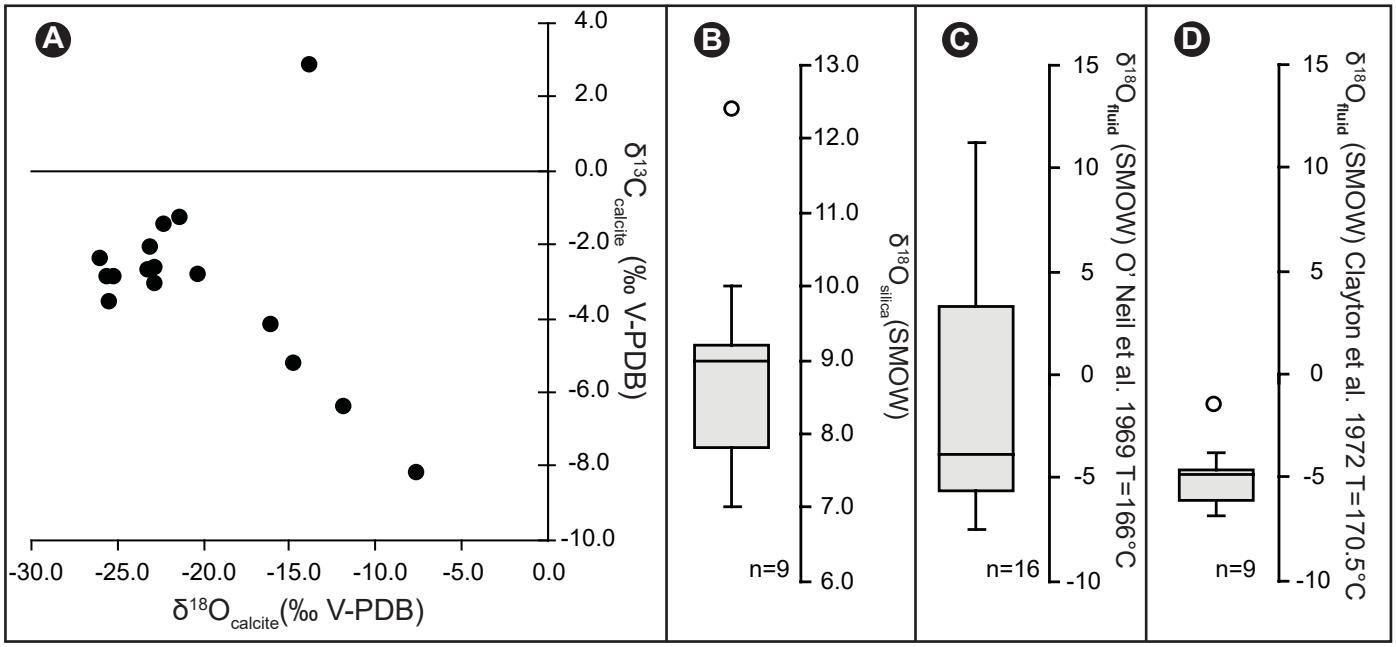
A
4.0
2.0
0.0
-2.0
-4.0
-6.0
-8.0
-10.0
δ13Ccalcite (‰ V-PDB)
-30.0
-25.0
-20.0
-15.0
-10.0
-5.0
0.0
δ18Ocalcite(‰ V-PDB)
B
13.0
12.0
11.0
10.0
9.0
8.0
7.0
6.0
δ18Osilica(SMOW)
n=9
C
15
10
5
0
-5
-10
δ18Ofluid (SMOW) O' Neil et al. 1969 T=166°C
n=16
D
15
10
5
0
-5
-10
δ18Ofluid (SMOW) Clayton et al. 1972 T=170.5°C
n=9

Figure 15

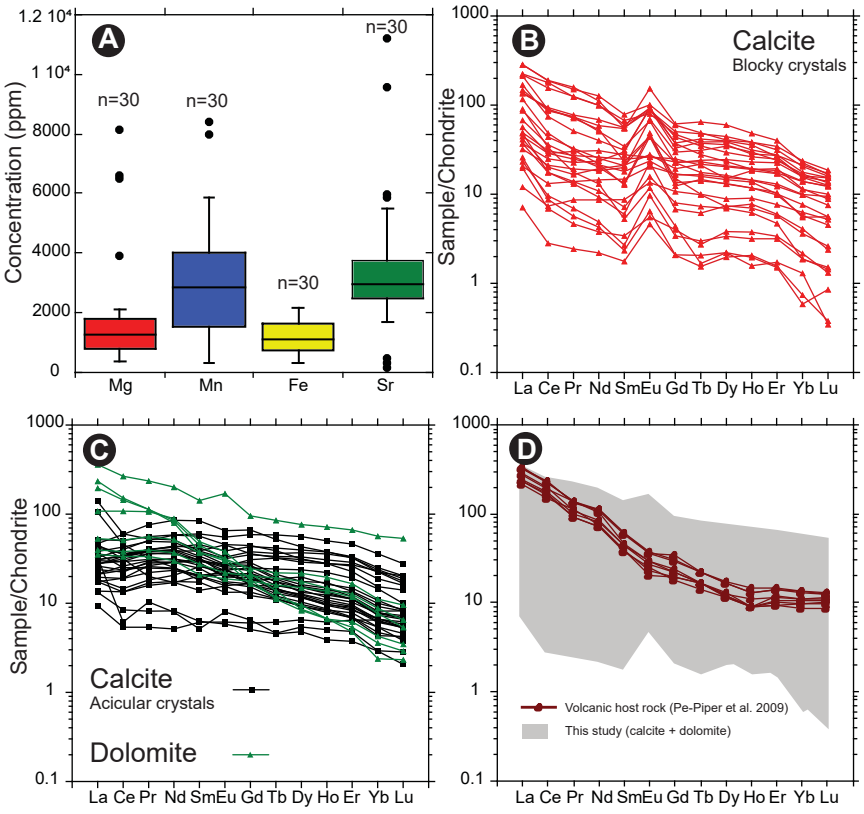
A
n=30
n=30
n=30
n=30
Concentration (ppm)
1.2 10⁴
1 10⁴
8000
6000
4000
2000
0
Mg
Mn
Fe
Sr
B
Calcite
Blocky crystals
Sample/Chondrite
1000
100
10
1
0.1
La Ce Pr Nd SmEu Gd Tb Dy Ho Er Yb Lu
C
Calcite
Acicular crystals
Dolomite
Sample/Chondrite
1000
100
10
1
0.1
La Ce Pr Nd SmEu Gd Tb Dy Ho Er Yb Lu
D
Volcanic host rock (Pe-Piper et al. 2009)
This study (calcite + dolomite)
1000
100
10
1
0.1
La Ce Pr Nd SmEu Gd Tb Dy Ho Er Yb Lu

Figure 16

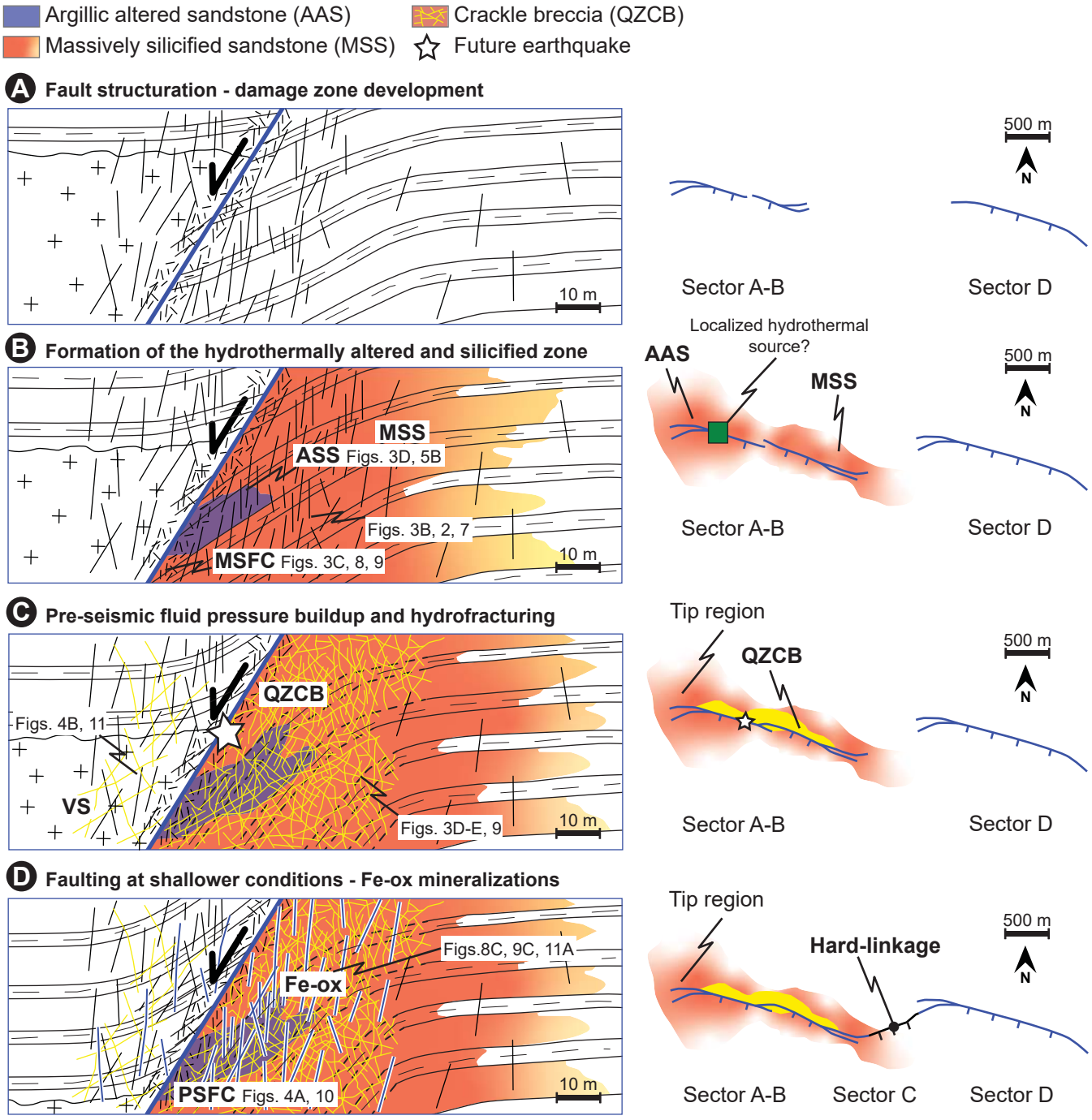
Argillic altered sandstone (AAS)
Crackle breccia (QZCB)
Massively silicified sandstone (MSS)
Future earthquake
A Fault structuration - damage zone development
10 m
500 m
N
Sector A-B
Sector D
B Formation of the hydrothermally altered and silicified zone
MSS
ASS Figs. 3D, 5B
Figs. 3B, 2, 7
MSFC Figs. 3C, 8, 9
10 m
Localized hydrothermal source?
AAS
MSS
C Pre-seismic fluid pressure buildup and hydrofracturing
QZCB
Figs. 4B, 11
VS
Figs. 3D-E, 9
Tip region
D Faulting at shallower conditions - Fe-ox mineralizations
Figs.8C, 9C, 11A
Fe-ox
PSFC Figs. 4A, 10
Hard-linkage
Sector C

TABLE 1. WHOLE-ROCK COMPOSITION OF HOST ROCKS AND HYDROTHERMALLY-ALTERED ROCKS FROM X-RAY DIFFRACTION ANALYSES

Sample Name	Fault-related rock/host rock	Distance from fault (m)	Phy	Qz	Cal	Dol	Ab	Kfs	Hl	Gth	Ant	Ap	Tr	
OK1	MSFC	0	0	80	-	-	-	20	-	-	-	-	-	
OK2	MSS	15	2	81	-	-	8	9	-	-	-	-	-	
OK4	QZCB (bulk)	38.5	3	82	-	-	6	9	-	-	-	-	-	
OK4	QZCB (clast)	38.5	11	68	-	-	13	8	-	-	-	-	-	
OK5	MSS	51.5	6	78	-	-	9	8	-	-	-	-	-	
OK6	MSS	72	7	63	-	-	20	10	-	-	-	-	-	
OK7	HR	128	16	48	4	-	26	7	-	-	-	-	-	
PK1	MSFC	0	9	72	-	-	1	18	-	-	-	-	-	
PK2	MSS	16.5	8	84	-	-	1	7	-	-	-	-	-	
PK3	MSS	21	6	81	-	-	2	11	-	-	-	-	-	
PK4	MSS	25	5	66	-	-	8	22	-	-	-	-	-	
PK5	MSS	38	9	74	-	-	6	11	-	-	-	-	-	
PK6	MSS	48	5	64	-	-	5	26	-	-	-	-	-	
PK7	MSS	57	9	88	-	-	3	-	-	-	-	-	-	
PK8	MSS	163	8	47	-	-	22	14	-	-	-	-	8	
PK9	MSS	170	16	84	-	-	-	-	-	-	-	-	-	
PK11	HR	180	18	53	-	-	19	10	-	-	-	-	-	
GV1	HR	5	5	55	15	-	14	12	-	-	-	-	-	
GV2	MSS	5	12	72	-	-	7	9	-	-	-	-	-	
PA1	MSS	79	0	89	-	-	11	-	-	-	-	-	-	
PA2	MSS	79	20	80	-	-	-	-	-	-	-	-	-	
PA3A	AAS	10	27	69	-	-	-	4	-	-	-	-	-	
S18	HR	>1000	48	17	26	5	2	tr	-	2	-	-	-	
S128	HR	>1000	47	17	22	9	2	tr	-	3	-	-	-	
SG33	PSFC	0	40	52	-	-	-	5	-	2	1	-	-	
SG34	PSFC	0	47	44	-	-	-	5	tr	2	2	-	-	
KOR K5	PSFC	0	42	55	-	-	-	tr	-	2	1	tr	-	
KOR K6	PSFC	0	47	50	-	tr	-	tr	-	2	1	tr	-	
KOR K7	PSFC	0	48	48	-	tr	-	1	-	2	1	tr	-	

Note: data are reported in wt. %. Phy: phyllosilicates, Qz: quartz, Cal: calcite, Dol: dolomite, Ab: albite, Kfs: K-feldspar, Hl: halite, Gth: goethite, Ant: anatase, Ap: apatite, tr: traces (<1%).
HR: host rock, PSFC: partially-silicified to non-silicified fault core rocks, MSS: massively silicified sandstones, MSFC: massively silicified fault core rocks, QZCB: quartz-cemented crackle breccias, AAS: argillic-altered sandstones.

TABLE 2. X-RAY DIFFRACTION ANALYSIS OF THE <2 μm GRAIN SIZE FRACTION

Sample name	Fault-related rock/host rock	Ilt	I-S	Chl	Kln	non-clay minerals	%Ilt in I-S	R
S18	HR	48	17	26	5	Qz, Cal, Dol, Ab, Kfs, Gth	30	0
S128	HR	47	17	22	9	Qz, Cal, Dol, Ab, Kfs, Gth	30	0
SG33	PSFC	40	52	-	-	Qz, Kfs, Gth	85	3
SG34	PSFC	47	44	-	-	Qz, Hl, Kfs, Gth	90	3
KOR K5	PSFC	42	55	-	-	Qz, Gth, Ant	90	3
KOR K6	PSFC	47	50	-	tr	Qz, Gth	90	3
KOR K7	PSFC	48	48	-	tr	Qz, Gth, Ant	90	3

Note: data are reported in wt. %. Ilt: illite, I-S: mixed layer illite-smectite, Chl: chlorite, Kln: kaolinite; Qz: quartz, Cal: calcite, Dol: dolomite, Ab: albite, Kfs: K-feldspar, Hl: halite, Gth: goethite, Ant: anatase, Tr: tremolite. tr: traces (<1%). HR: host rock, PSFC: partially-silicified to non-silicified fault core rocks. R=stacking order (Jagodzinski, 1949).

TABLE 3. MICROTHERMOMETRIC DATA OF CALCITE AND SILICA CEMENTS

Mineral phase	Size range (μm)	L/V range	Th range (°C)	Th mean (°C)	$Tm_{ice/cla}$ range (°C)	$Tm_{ice/cla}$ mean (°C)
Calcite	4 to 20	5 to 20	132 to 198	166	-1.4 to 15.9	0.6
Quartz	4 to 20	5 to 20	136 to 203	170	-1.5 to 5.3	0.0

Note: L: liquid, V: vapor, Th: homogenization temperature, $Tm_{ice/cla}$: melting temperature of ice/clathrates

TABLE 4. CARBON AND OXYGEN STABLE ISOTOPE DATA

	Mineral									Fluid		
	$\delta^{18}O$ (V-PDB)			$\delta^{13}C$ (V-PDB)			$\delta^{18}O$ (SMOW)			$\delta^{18}O$ (SMOW)		
	Range	Mean	St. Dev	Range	Mean	St. Dev	Range	Mean	St. Dev	Range	Mean	St. Dev
Calcite n=16	-26.1 to -7.7	-20.2	5.6	-8.2 to 2.9	-3.0	2.4	4.0 to 23.0	10.1	2.4	-7.5 to 11.3	-1.5	5.6
Silica cements n=9	/	/	/	/	/	/	7 to 12.4	8.9	1.6	-6.8 to -1.37	-4.9	1.6

Note: V-PDB: Vienna-Pee Dee Belemnite, SMOW: Standard Mean Ocean Water, St. Dev.: Standard Deviation

TABLE 5. HYDROGEN STABLE ISOTOPE DATA OF WHOLE-ROCK AND <2µm GRAIN SIZE FRACTION

Sample ID	Fault-related rock/host rock	whole-rock samples (‰)		<2µm grain size fraction (‰)	
		δD	δDw	δD	δDw
S18	HR	-90.3	-83.9	-75.1	-68.6
S128	HR	-82.7	-78.4	-67.1	-59.4
SG33	PSFC	-101.9	-94.2	-82.3	-75.0
SG34	PSFC	-92.4	-86.9	-87.3	-80.8
KOR K5	PSFC	-91.5	-88.4	-83.9	-80.4
KOR K6	PSFC	-141.6	-138.0	-72.9	-69.0
KOR K7	PSFC	-91.7	-88.0	-74.2	-69.8

Note: the standard deviation of each measurement is <3‰ for the whole-rock samples and <1‰ for the <2µm grain size fraction.
δDw: calculated δD signature of the fluid.